

Phase Field Models versus Parametric Front Tracking Methods: Are they accurate and computationally efficient?

John W. Barrett[†] Harald Garcke[‡] Robert Nürnberg[†]

Abstract

We critically compare the practicality and accuracy of numerical approximations of phase field models and sharp interface models of solidification. Particular emphasis is put on Stefan problems, and their quasi-static variants, with applications to crystal growth. New approaches with a high mesh quality for the parametric approximations of the resulting free boundary problems and new stable discretizations of the anisotropic phase field system are taken into account in a comparison involving benchmark problems based on exact solutions of the free boundary problem.

Key words. phase field models, parametric sharp interface methods, Stefan problem, anisotropy, solidification, crystal growth, numerical simulations, benchmark problems

AMS subject classifications. 35K55, 35R35, 35R37, 53C44, 65M12, 65M50, 65M60, 74E10, 74E15, 74N20, 80A22, 82C26

1 Introduction

The solidification of a liquid or the melting of a solid lead to complex free boundary problems involving many different physical effects. For example, latent heat is set free at the interface and a competition between surface energy and diffusion leads to instabilities like the Mullins–Sekerka instability. The resulting model is a Stefan problem with boundary conditions taking surface energy effects and kinetic effects at the interface into account, see e.g. [49, 35]. Crystals forming in an undercooled melt lead to very complex patterns and, in particular, dendritic growth can be observed since the growth is typically diffusion limited, see [19].

[†]Department of Mathematics, Imperial College London, London, SW7 2AZ, UK

[‡]Fakultät für Mathematik, Universität Regensburg, 93040 Regensburg, Germany

The numerical simulation of time-dependent Stefan problems, or variants of it, is a formidable task since the evolving free boundary has to be computed. Hence, direct front tracking type numerical methods need to adequately capture the geometry of the interface and to evolve the interface approximation, often with a coupling to other physical fields. This coupling, in particular, represents a significant initial hurdle towards obtaining practical implementations, and thus numerical simulations for the problem at hand. Examples of the implementation of such direct methods can be found in e.g. [54, 77, 5, 2, 69, 68, 70, 51, 71, 12].

A further drawback of direct front tracking methods has been the inability of most direct methods to deal with so-called mesh effects, or to prevent them altogether. When a discrete approximation of an interface, for example a polygonal curve in the plane, evolves in time, then in general it is possible for the approximation to deteriorate or to break down. Examples of such pathologies are self-crossings and vertex coalescence. While for simple isotropic problems in the plane these issues can be dealt with, for example by frequent remeshings or by using clever formulations that only allow equidistributed approximations, see e.g. [54, 77], until very recently there has been no remedy for fully anisotropic problems in two and three space dimensions.

However, building on their work for isotropic problems in [8, 7, 10], the present authors recently introduced stable parametric finite element schemes for the direct approximation of anisotropic geometric evolution equations in [9, 11], for which good mesh properties can be guaranteed. In particular, even for the simulation of interface evolutions in the presence of strong anisotropies, no remeshing or redistribution of vertices is needed in practice. These schemes, in which only the interface without a coupling to bulk quantities is modelled, have been extended to approximations of the Stefan problem with fully anisotropic Gibbs–Thomson law and kinetic undercooling in [12]. The novel method from [12] can be shown to be stable and to have good mesh properties. We remark that these approaches extend earlier ideas from [37, 69, 70]. Here we recall the pioneering work of Schmidt [69, 70], where the full Stefan problem in three dimensions was solved within a sharp interface framework for the first time.

Phase field methods are an alternative approach to solve solidification phenomena in the framework of continuum modelling. In phase field approaches a new non-conserved order parameter φ is introduced, which in the two phases is close to two different prescribed values and which smoothly changes its value across a small diffuse interfacial region. A parabolic partial differential equation for φ is then coupled to an energy balance, which results in a diffusion equation for the temperature taking latent heat effects into account. We refer to [56, 34, 25, 66, 79] and to the five review articles [24, 31, 59, 73, 75] for further details. In particular, it can be shown that solutions to the phase field equations converge to classical sharp interface problems, see e.g. [26, 1, 74, 27] and the references therein.

The popularity of phase field methods, often also called diffuse interface methods, can be explained by two characteristic features that they share with the level set method, which is another sharp interface computational tool. Firstly, phase field methods naturally allow for changes of topology. And secondly, computing simulations for phase field models only

requires the solution of partial differential equations on standard Cartesian domains. The fact that these can usually be implemented and solved in a relatively straightforward way makes the phase field method particularly appealing.

It is the aim of this article to investigate the practical merits of phase field models compared to the recently introduced sharp interface algorithm for the approximation of Stefan problems from [12]; see also [13, 14]. Of particular interest will be the relative accuracy of the two methods, in situations where a true solution to the sharp interface problem is known. In a phase field simulation the observed error is made up of contributions from

- the asymptotic error,
- the spatial and temporal discretization errors,
- rounding errors and solver tolerances.

Here the asymptotic error is induced by the choice of interfacial parameter $\varepsilon > 0$. In general one can formally show that the asymptotic error converges to zero as $\varepsilon \rightarrow 0$, see e.g. [25]. For certain phase field models and under certain conditions it can be rigorously shown that the asymptotic error vanishes as $\varepsilon \rightarrow 0$, see e.g. [27]. In computations for sharp interface approximations, on the other hand, the observed error is made up of the latter two contributions only, i.e. of discretization and rounding errors. A disadvantage of phase field models is that the resulting PDEs become stiff for decreasing ε , leading to a requirement for very fine spatial and temporal discretizations. Hence it becomes computationally challenging to produce very accurate phase field simulations. In any case, the available computational resources will often set a limit on the smallest interfacial parameter ε that one can compute for. Hence another aspect that needs to be taken into account in an objective comparison between phase field simulations and sharp interface approximations is the overall CPU time that is needed to obtain the results. While it can often be formally shown that phase field computations can attain an arbitrarily high accuracy, the existing limitations on computer hardware often mean that in practice very fine computations cannot be performed. In addition, as discussed in [52], the early computational approaches were limited as they could only be used in the presence of interfacial kinetics in the Gibbs–Thomson law.

Historically these limitations of the phase field model have long been known, and as a result a different underlying interpretation of the model, the so-called “thin interface limit”, has been introduced and analyzed by Karma and Rappel [52, 53]. Their approach made it possible to do efficient computations with a smaller capillary length to interface thickness ratio, and to study the physically relevant case of small or zero kinetic coefficients. Later the findings of Karma and Rappel were reinterpreted as second order convergence with respect to the interfacial thickness, see [3, 45, 32].

The first successful phase field computations of dendritic growth were performed by Kobayashi [55], and his computations demonstrated the importance of anisotropy for dendritic growth. Since then many successful improvements with respect to numerical simu-

lations have appeared in the literature. We refer to [41, 80, 52, 67, 62] and the references therein.

Finally, we would like to mention work on the numerical analysis of phase field and sharp interface approaches. Numerical analysis of discretizations of phase field models can be found in e.g. [29, 44, 57, 33, 81, 43, 17]. Numerical analysis of discretizations of sharp interface models can be found in [78, 12, 13]. We also remark that level set methods are another possible way to solve Stefan problems and related free boundary problems. We refer to [65, 72] for more details on how the level set method can be used to solve free boundary problems.

The remainder of the paper is organized as follows. In Section 2 we state the sharp interface formulation of the two phase Stefan problem with kinetic undercooling and an anisotropic Gibbs–Thomson law. In Section 3 we state the corresponding phase field model and recall the finite element algorithms from [16]. In Section 4 we numerically compare the sharp interface method from [12] with the phase field algorithms from Section 3 for some isotropic benchmark problems with known true solutions. Computations for a phase field model with a correction term, for which a second order convergence property can formally be shown, are presented in Section 4.3. Finally, we compare the sharp interface and phase field methods for a variety of anisotropic model problems in Section 5.

2 Sharp interface problem

In this paper we concentrate on interfacial problems in materials science in which one driving force is due to capillary effects. In applications the interface often separates a solid and a liquid phase, say, or a solid phase and a gas phase. Let $\Gamma(t) \subset \mathbb{R}^d$, $d = 2, 3$, denote this sharp interface. Then the surface energy of $\Gamma(t)$ is defined as

$$\int_{\Gamma(t)} \gamma(\mathbf{n}) \, ds, \quad (2.1)$$

where \mathbf{n} denotes the unit normal of $\Gamma(t)$, and where the anisotropic density function $\gamma : \mathbb{R}^d \rightarrow \mathbb{R}_{\geq 0}$ with $\gamma \in C^2(\mathbb{R}^d \setminus \{0\}) \cap C(\mathbb{R}^d)$ is assumed to be absolutely homogeneous of degree one, i.e.

$$\gamma(\lambda p) = |\lambda| \gamma(p) \quad \forall p \in \mathbb{R}^d, \forall \lambda \in \mathbb{R} \quad \Rightarrow \quad \gamma'(p) \cdot p = \gamma(p) \quad \forall p \in \mathbb{R}^d \setminus \{0\},$$

with γ' denoting the gradient of γ . For all the considerations in this paper we assume that γ is of the class of anisotropies first introduced by the authors in [9, 11]; see also [12, 16].

Relevant for our considerations is the first variation, $-\kappa_\gamma$, of (2.1), which can be computed as

$$\kappa_\gamma := -\nabla_s \cdot \gamma'(\mathbf{n});$$

where $\nabla_s \cdot$ is the tangential divergence of Γ , see e.g. [30, 11, 12]. Note that κ_γ reduces to κ , the sum of the principal curvatures of Γ , in the isotropic case, i.e. when γ satisfies

$$\gamma(p) = |p| \quad \forall p \in \mathbb{R}^d. \quad (2.2)$$

2.1 Stefan problem

Then the full Stefan problem we want to consider in this paper is given as follows, where $\Omega \subset \mathbb{R}^d$ is a given fixed domain with boundary $\partial\Omega$ and outer normal ν . Find $u : \Omega \times [0, T] \rightarrow \mathbb{R}$ and the interface $(\Gamma(t))_{t \in [0, T]}$ such that for all $t \in (0, T]$ the following conditions hold:

$$\vartheta u_t - \mathcal{K}_- \Delta u = 0 \quad \text{in } \Omega_-(t), \quad \vartheta u_t - \mathcal{K}_+ \Delta u = 0 \quad \text{in } \Omega_+(t), \quad (2.3a)$$

$$\left[\mathcal{K} \frac{\partial u}{\partial \mathbf{n}} \right]_{\Gamma(t)} = -\lambda \mathcal{V} \quad \text{on } \Gamma(t), \quad (2.3b)$$

$$\frac{\rho \mathcal{V}}{\beta(\mathbf{n})} = \alpha \kappa_\gamma - a u \quad \text{on } \Gamma(t), \quad (2.3c)$$

$$\frac{\partial u}{\partial \nu} = 0 \quad \text{on } \partial_N \Omega, \quad u = u_D \quad \text{on } \partial_D \Omega, \quad (2.3d)$$

$$\Gamma(0) = \Gamma_0, \quad \vartheta u(\cdot, 0) = \vartheta u_0 \quad \text{in } \Omega. \quad (2.3e)$$

In the above u denotes the deviation from the melting temperature T_M , i.e. T_M is the melting temperature for a planar interface. In addition, $\Omega_-(t)$ is the solid region, with boundary $\Gamma(t) = \partial\Omega_-(t)$, so that the liquid region is given by $\Omega_+(t) := \Omega \setminus \Omega_-(t)$. Moreover, here and throughout this paper, for a quantity v defined on Ω , we use the shorthand notations $v_- := v|_{\Omega_-}$ and $v_+ := v|_{\Omega_+}$. The parameters $\vartheta \geq 0$, $\lambda > 0$, $\rho \geq 0$, $\alpha > 0$, $a > 0$ are assumed to be constant, while $\mathcal{K} > 0$ is assumed to be constant in each phase. The mobility coefficient $\beta : \mathbb{R}^d \rightarrow \mathbb{R}_{\geq 0}$ is assumed to satisfy $\beta(p) > 0$ for all $p \neq 0$ and to be positively homogeneous of degree one. We note that in the isotropic case (2.2) it is often also assumed that

$$\beta(p) = |p| \quad \forall p \in \mathbb{R}^d \quad \Rightarrow \quad \beta(\mathbf{n}) = 1. \quad (2.4)$$

In addition $[\mathcal{K} \frac{\partial u}{\partial \mathbf{n}}]_{\Gamma(t)}(z) := (\mathcal{K}_+ \frac{\partial u_+}{\partial \mathbf{n}} - \mathcal{K}_- \frac{\partial u_-}{\partial \mathbf{n}})(z)$ for all $z \in \Gamma(t)$, and \mathcal{V} is the velocity of $\Gamma(t)$ in the direction of its normal \mathbf{n} , which from now on we assume is pointing into $\Omega_+(t)$. Finally, $\partial\Omega = \partial_N \bar{\Omega} \cup \partial_D \bar{\Omega}$ with $\partial_N \bar{\Omega} \cap \partial_D \bar{\Omega} = \emptyset$, $u_D \in \mathbb{R}_{\leq 0}$ is the applied supercooling at the boundary, and $\Gamma_0 \subset \bar{\Omega}$ and $u_0 : \Omega \rightarrow \mathbb{R}$ are given initial data. Here we use the convention that $u_D = 0$ if $\partial\Omega = \partial_N \bar{\Omega}$.

The model (2.3a–e) can be derived for example within the theory of rational thermodynamics and we refer to [48] for details. We remark that a derivation from thermodynamics would lead to the identity $a = \frac{\lambda}{T_M}$. We note that (2.3b) is the well-known Stefan condition, while (2.3c) is the Gibbs–Thomson condition, with kinetic undercooling if $\rho > 0$. The case $\vartheta > 0$, $\rho > 0$, $\alpha > 0$ leads to the Stefan problem with the Gibbs–Thomson law and kinetic undercooling. In some models in the literature, see e.g. [58], the kinetic undercooling is set to zero, i.e. $\rho = 0$. Setting $\vartheta = \rho = 0$ but keeping $\alpha > 0$ leads to the Mullins–Sekerka problem with the Gibbs–Thomson law, see [61].

We recall from [12] that for a solution u and Γ to (2.3a–e) it can be shown that the following equality holds

$$\frac{d}{dt} \mathcal{F}(\Gamma, u) = -(\mathcal{K} \nabla u, \nabla u) - \frac{\lambda \rho}{a} \int_{\Gamma(t)} \frac{\mathcal{V}^2}{\beta(\mathbf{n})} ds \leq 0, \quad (2.5)$$

where

$$\mathcal{F}(\Gamma, u) := \frac{\vartheta}{2} |u - u_D|_0^2 + \frac{\lambda \alpha}{a} \int_{\Gamma(t)} \gamma(\mathbf{n}) \, ds - \lambda u_D |\Omega_+(t)| \quad (2.6)$$

and where (\cdot, \cdot) denotes the L^2 -inner product over Ω , with the corresponding norm given by $|\cdot|_0$, and where $|\Omega_+(t)| := \int_{\Omega_+(t)} 1 \, dx$.

2.2 Parametric method PFEM

Traditional front tracking methods for sharp interface problems had a major drawback, in that the meshes used to describe the interface seriously deteriorated during the evolution. In addition, introducing mesh smoothing during the evolution is difficult, see e.g. the discussion in [70]. For interfaces in the plane it is possible to formulate a non-trivial method such that mesh points are nearly equally distributed during the evolution, see [50, 60]. The present authors introduced a novel parametric finite element method for problems involving curves and surfaces evolving in time, which has a simple variational structure and which leads to good mesh properties, see [8, 7, 10]. In fact, for curves a semi-discrete variant leads to equally distributed mesh points in the isotropic case, while in the general anisotropic setting equidistribution with respect to some anisotropic weight function is obtained, see [9]. For surfaces the resulting meshes have also good properties, which in the isotropic case can be explained by using ideas from conformal geometry. In particular, no remeshing is needed during the evolution, even in the general anisotropic situation. An example triangulation obtained during the simulation of dendritic growth in three space dimensions can be seen in Figure 21, below. In addition, as the mesh for the parameterization of the interface is decoupled from the bulk mesh, no deformation of the bulk mesh is required in order to contain the interface at predefined locations on it.

The novel and stable parametric finite element approximation of (2.3a–e) in the case $\mathcal{K}_+ = \mathcal{K}_- > 0$ has been introduced by the present authors in [12], and this scheme has been extended to the more general case $\mathcal{K}_\pm \geq 0$ in [13]. Throughout this paper we will refer to these variants as PFEM. The algorithm PFEM features the discretization parameters h_Γ , h_f , h_c and τ . Here h_Γ refers to the fineness of the triangulated approximation of $\Gamma(t)$, for which isoparametric piecewise linear finite elements are employed. In particular, a simple mesh refinement strategy allows for the natural growth of the interface, i.e. elements of the triangulated approximation of $\Gamma(t)$ are refined when they become too large. Moreover, the temperature in the bulk is approximated with standard continuous piecewise linear finite elements, and h_f and h_c refer to bulk mesh parameters for fine regions close to the interface and coarser regions far away from it. For all the computations presented in this paper we fix $h_c = 8 h_f$ and, unless stated otherwise, we let $h_f \approx h_\Gamma$. Finally, τ denotes a uniform time step size. The linear discrete systems of equations are solved with preconditioned conjugate gradient solvers of suitable Schur complement formulations. We refer to [12, 13] for more details. As indicated earlier, no remeshing of the discrete interface is necessary for the scheme PFEM, and all the numerical results presented in this paper for this scheme are performed without any redistribution of mesh points.

3 Phase field model

We now state the phase field model that we are going to consider in this paper. To this end, for $p \in \mathbb{R}^d$, let

$$A(p) = \frac{1}{2} |\gamma(p)|^2 \quad \Rightarrow \quad A'(p) = \begin{cases} \gamma(p) \gamma'(p) & p \neq 0, \\ 0 & p = 0, \end{cases}$$

and define

$$\mu(p) = \begin{cases} \frac{\gamma(p)}{\beta(p)} & p \neq 0, \\ \bar{\mu} & p = 0, \end{cases} \quad (3.1)$$

where $\bar{\mu} \in \mathbb{R}_{>0}$ is a constant satisfying $\min_{p \neq 0} \frac{\gamma(p)}{\beta(p)} \leq \bar{\mu} \leq \max_{p \neq 0} \frac{\gamma(p)}{\beta(p)}$.

Moreover, let $\varphi : \Omega \times (0, T) \rightarrow \mathbb{R}$ be the phase field variable, so that the sets $\{x \in \Omega : \pm \varphi(x, t) > 0\}$ are approximations to $\Omega_{\pm}(t)$, with the zero level set of $\varphi(\cdot, t)$ approximating the interface $\Gamma(t)$. On introducing the small interfacial parameter $\varepsilon > 0$, it can be shown that

$$\frac{1}{c_{\Psi}} \mathcal{E}_{\varepsilon}(\varphi) \approx \int_{\Gamma} \gamma(n) \, ds,$$

for ε sufficiently small, where

$$\mathcal{E}_{\varepsilon}(\varphi) := \int_{\Omega} \frac{\varepsilon}{2} |\gamma(\nabla \varphi)|^2 + \varepsilon^{-1} \Psi(\varphi) \, dx \quad \text{with} \quad c_{\Psi} := \int_{-1}^1 \sqrt{2 \Psi(s)} \, ds. \quad (3.2)$$

Here $\Psi : \mathbb{R} \rightarrow [0, \infty]$ is a double well potential, which we assume to be symmetric and to have its global minima at ± 1 . The canonical example is

$$\Psi(s) := \frac{1}{4} (s^2 - 1)^2 \quad \Rightarrow \quad \Psi'(s) = s^3 - s \quad \text{and} \quad c_{\Psi} = \frac{1}{3} 2^{\frac{3}{2}}. \quad (3.3)$$

Another possibility is to choose

$$\Psi(s) := \begin{cases} \frac{1}{2} (1 - s^2) & |s| \leq 1, \\ \infty & |s| > 1, \end{cases} \quad \Rightarrow \quad c_{\Psi} = \frac{\pi}{2}; \quad (3.4)$$

see e.g. [22, 23, 41, 40]. Clearly the obstacle potential (3.4), which in contrast to the smooth quartic potential (3.3) forces φ to stay within the interval $[-1, 1]$, is not differentiable at ± 1 . Hence, whenever we write $\Psi'(s)$ in the case (3.4) in this paper, we mean that the expression holds only for $|s| < 1$, and that in general a variational inequality needs to be employed.

Our phase field model for (2.3a–e) is then given by the coupled system

$$\vartheta w_t + \lambda \varrho(\varphi) \varphi_t - \nabla \cdot (b(\varphi) \nabla w) = 0 \quad \text{in } \Omega_T := \Omega \times (0, T), \quad (3.5a)$$

$$w = u_D \quad \text{on } \partial_D \Omega \times (0, T), \quad (3.5b)$$

$$b(\varphi) \frac{\partial w}{\partial \nu} = 0 \quad \text{on } \partial_N \Omega \times (0, T), \quad (3.5c)$$

$$\vartheta w(\cdot, 0) = \vartheta w_0 \quad \text{in } \Omega, \quad (3.5d)$$

with

$$c_\Psi \frac{a}{\alpha} \varrho(\varphi) w = \varepsilon \frac{\rho}{\alpha} \mu(\nabla \varphi) \varphi_t - \varepsilon \nabla \cdot A'(\nabla \varphi) + \varepsilon^{-1} \Psi'(\varphi) \quad \text{in } \Omega_T, \quad (3.6a)$$

$$\frac{\partial \varphi}{\partial \nu} = 0 \quad \text{on } \partial\Omega \times (0, T), \quad (3.6b)$$

$$\varphi(\cdot, 0) = \varphi_0 \quad \text{in } \Omega, \quad (3.6c)$$

where

$$b(s) = \frac{1}{2} (1 + s) \mathcal{K}_+ + \frac{1}{2} (1 - s) \mathcal{K}_-,$$

and where the function $\varrho \in C^1(\mathbb{R})$ is such that

$$\varrho(s) \geq 0 \quad \forall s \in [-1, 1], \quad \int_{-1}^1 \varrho(y) dy = 1 \quad \text{and} \quad P(s) := \int_{-1}^s \varrho(y) dy. \quad (3.7)$$

We note that P , which is a monotonically increasing function over the interval $[-1, 1]$ with $P(-1) = 0$ and $P(1) = 1$, is often called the interpolation function. In this paper, we follow the convention from [41], where $\varrho = P'$ is called the shape function. Possible choices of ϱ that will be considered in this paper are

$$(i) \varrho(s) = \frac{1}{2}, \quad (ii) \varrho(s) = \frac{1}{2} (1 - s), \quad (iii) \varrho(s) = \frac{15}{16} (s^2 - 1)^2, \quad (iv) \varrho(s) = \frac{3}{4} (1 - s^2). \quad (3.8)$$

More details on interpolation functions P , respectively shape functions ϱ , can be found in e.g. [79, 45, 28]. In particular, if one also assumes that ϱ is symmetric, i.e.

$$\varrho(s) = \varrho(-s) \quad \forall s \in \mathbb{R}, \quad (3.9a)$$

and that

$$\varrho(1) = \varrho(-1) = 0, \quad (3.9b)$$

then a faster rate of convergence of the phase field model to the sharp interface limit, as $\varepsilon \rightarrow 0$, can be shown in the isotropic case (2.2), (2.4) on replacing ρ in (3.6a) with the first order correction

$$\widehat{\rho} := \rho + \varepsilon \rho_1, \quad (3.10)$$

where ρ_1 is defined in (4.7) in Section 4.3, below. The condition (3.9b) is one motivation for the latter two choices in (3.8), with the choice (3.8)(iv) also satisfying the stronger condition (4.9), below, for the quartic potential (3.3). An error analysis for a fully discrete approximation of the phase field model (3.5a–d), (3.6a–c) with the quartic potential (3.3) and the shape function (3.8)(i) in the isotropic case (2.2), (2.4) with $\partial_N \Omega = \partial\Omega$ and $\mathcal{K}_+ = \mathcal{K}_- > 0$ has been performed in [43]. These authors also show convergence of the phase field discretizations to the underlying sharp interface problem as $\varepsilon, h, \tau \rightarrow 0$, where h and τ denote the discretization parameters in space and time, respectively. However, to our knowledge, no convergence rates are known for the convergence of discretizations of the phase field model to the sharp interface problem (2.3a–e). Here we recall that for the much simpler situation of planar curvature flow, as the sharp interface limit of the isotropic Allen–Cahn equation, such convergence rates have been obtained in [64]. In particular, it can be shown that the zero level sets of discretizations of

$$\varepsilon \varphi_t = \varepsilon \Delta \varphi - \varepsilon^{-1} \Psi'(\varphi)$$

for the obstacle potential (3.4) converge with $\mathcal{O}(\varepsilon)$ to the sharp interface limit moving by $\mathcal{V} = \kappa$ if

$$\tau = \mathcal{O}(h^2) = \mathcal{O}(\varepsilon^4). \quad (3.11)$$

While no such result is known for the full phase field model (3.5a–d), (3.6a–c) even in the isotropic setting, it is natural to expect constraints of the form (3.11) in order to observe $\mathcal{O}(\varepsilon)$ in practice.

We remark that the phase field analogue of the sharp interface energy identity (2.5) is given by the formal energy bound

$$\frac{d}{dt} \mathcal{F}_\varepsilon(\varphi, w) = -(b(\varphi) \nabla w, \nabla w) - \varepsilon \frac{\lambda \rho}{a} \frac{1}{c_\Psi} (\mu(\nabla \varphi), (\varphi_t)^2) \leq 0 \quad (3.12)$$

for the phase field model (3.5a–d), (3.6a–c), where

$$\mathcal{F}_\varepsilon(\varphi, w) := \frac{\vartheta}{2} |w - u_D|_0^2 + \frac{\lambda \alpha}{a} \frac{1}{c_\Psi} \mathcal{E}_\varepsilon(\varphi) - \lambda u_D \int_\Omega P(\varphi) \, dx. \quad (3.13)$$

Phase field models that satisfy such an inequality, in analogy to the sharp interface energy identity (2.5), are often called thermodynamically consistent, see [66, 79, 45].

3.1 Phase field methods PF^{obs} -FEM and PF^{qua} -FEM

Unconditionally stable, fully practical finite element approximations of (3.5a–d), (3.6a–c) with either (3.3) or (3.4) have been introduced by the authors in [16]. Here stable means that they satisfy a discrete analogue of the formal energy bound (3.12). Throughout this paper we will refer to the approximations from [16] for (3.3) and (3.4) as PF^{qua} -FEM and PF^{obs} -FEM, respectively, where the inclusion of a subscript refers to the choice of shape function in (3.8), e.g. $\text{PF}_{(i)}^{\text{obs}}$ -FEM. We recall from [16] that a side effect of the interpolation function P in (3.13) is that the function

$$G(s) = \alpha (a c_\Psi \varepsilon)^{-1} \Psi(s) - u_D P(s)$$

need no longer have local minima at $s = \pm 1$ if $u_D \neq 0$. This can result, for example, in undesired, artificial boundary layers for strong supercoolings, i.e. when $-u_D$ is large. For the smooth potential Ψ from (3.3), sufficient conditions for $s = \pm 1$ to be local minimum points of $G(s)$ are

$$\varrho(\pm 1) = \varrho'(\pm 1) = 0, \quad (3.14)$$

which is evidently satisfied by (3.8)(iii). In fact, in applications phase field models for solidification almost exclusively use this shape function; see e.g. [24, 31, 59]. For the obstacle potential (3.4) the situation is similar, although there is more flexibility in the possible choices of ϱ . In particular, here a sufficient condition for $G(s)$ to have local minima at $s = \pm 1$ is given by

$$\alpha (a c_\Psi \varepsilon)^{-1} \pm u_D \varrho(\pm 1) \geq 0. \quad (3.15)$$

On recalling that $u_D \leq 0$ we see that for (3.15) to hold it is sufficient to require that $\varrho(1) = 0$, which is evidently satisfied by (3.8)(ii), (3.8)(iii) and (3.8)(iv). A major advantage of (3.8)(ii) over (3.8)(iii) and (3.8)(iv) is that for (3.8)(ii) it is possible to derive almost linear finite element approximations that are unconditionally stable. The corresponding unconditionally stable schemes for the nonlinear shape functions (3.8)(iii) and (3.8)(iv), on the other hand, turn out to be highly nonlinear. See [16] for more details.

We remark that even when (3.14) and (3.15) are satisfied for the potentials (3.3) and (3.4), respectively, it is possible that mushy interfacial regions are observed in practice for approximations of the phase field model (3.5a–d), (3.6a–c); see e.g. Figure 13, below. That is particularly the case in situations where the instability of the moving free boundary is strong, i.e. when $-u_D a \alpha^{-1}$ is large, recall (2.6) and see e.g. [61]. Then ε needs to be chosen small, recall (3.13), so that the phase field variable φ admits well-defined interfacial regions that approximate the sharp interface $\Gamma(t)$. This gives rise to a formal constraint of the form

$$\varepsilon \leq C \alpha (-u_D a)^{-1} \quad \text{if } u_D < 0, \quad (3.16)$$

for the choice of the interfacial parameter ε in terms of the physical parameters for the sharp interface problem (2.3a–e), irrespective of the choice of ϱ . The reason for this is that in the estimate (3.12) the double well term $\varepsilon^{-1} \int_{\Omega} \Psi(\varphi) \, dx$ in $\mathcal{E}_{\varepsilon}(\varphi)$ is for large ε not strong enough to bound the unstable term involving $P(\varphi)$, which encourages the growth of the diffuse interface.

The two algorithms PF^{obs}-FEM and PF^{qua}-FEM, which use continuous piecewise linear finite elements in space, feature the discretization parameters h_f , h_c and τ . Here h_f and h_c are mesh parameters for fine triangulations inside the diffuse interfacial region and coarser triangulations far away from it. Meaningful phase field simulations need to resolve the interfacial regions, whose width is of the order ε , and so a constraint of the form

$$h_f \leq C \varepsilon \quad (3.17)$$

needs to be enforced. For (3.4) the asymptotic interface width is $\pi \varepsilon$ in the isotropic case (2.2), and in this paper we always choose $h_f \leq \frac{\pi \varepsilon}{8}$ with $h_c = 8 h_f \leq \pi \varepsilon$. Unless otherwise stated we let $h_f = \frac{\pi \varepsilon}{8}$. Finally, τ denotes a uniform time step size. Here we recall that the schemes PF^{obs}-FEM and PF^{qua}-FEM employ a semi-implicit discretization in time, which utilizes convex/concave splittings of the nonlinearity arising from the potential Ψ and from the interpolation function P . Such a splitting for Ψ was first proposed in [42], see also [6], and the idea generalizes naturally to P ; see Section 3.2, below, for details. This means that for the shape function choices (3.8)(i) and (3.8)(ii) almost linear schemes are obtained, while the choices (3.8)(iii) and (3.8)(iv) give rise to more nonlinear finite element approximations; see [16] for details. The discrete systems of linear equations and variational inequalities arising from the schemes PF^{obs}-FEM are solved with the Uzawa-multigrid solver from [4], while the systems of nonlinear equations arising from PF^{qua}-FEM are solved with a Newton method. We refer to [16] for more details.

For completeness we briefly describe the choice of the initial profile φ_0 in (3.6c) in our numerical computations. Given the initial interface Γ_0 from (2.3e), we let $d_0 : \Omega \rightarrow \mathbb{R}$

denote the signed distance function of Γ_0 . Then, on recalling the asymptotic phase field profiles from e.g. [40], we define

$$\varphi_0(x) = \Phi(\varepsilon^{-1} d_0(x)), \quad \text{where} \quad \Phi(s) := \begin{cases} -1 & s \leq -\frac{\pi}{2}, \\ \sin(s) & |s| < \frac{\pi}{2}, \\ 1 & s \geq \frac{\pi}{2}, \end{cases} \quad (3.18a)$$

for the obstacle potential (3.4), while for the smooth quartic potential (3.3) we use

$$\varphi_0(x) = \Phi(\varepsilon^{-1} d_0(x)), \quad \text{where} \quad \Phi(s) := \tanh(2^{-\frac{1}{2}} s). \quad (3.18b)$$

For simplicity we use the profiles (3.18a,b) also in the anisotropic setting, where it would be more appropriate to replace d_0 with a suitably defined anisotropic distance function d_γ , see [36] for details. Finally, if $\vartheta > 0$, we fix $w_0 = u_0$.

3.2 Possible time discretizations

In Section 4 we will investigate the accuracy and the efficiency of several discretizations of the phase field model (3.5a–d), (3.6a–c) in the isotropic case (2.2), (2.4). In addition to the schemes PF^{obs}-FEM and PF^{qua}-FEM from [16], which use a semi-implicit discretization in time, we will also look at a more implicit discretization and at a fully explicit discretization. For later reference, we now state the three different time discretizations, and for simplicity we do so on ignoring spatial discretization. A strong formulation of the time discretization from [16] is given as follows. Let $\Psi = \Psi^+ + \Psi^-$, with Ψ^+ being convex on \mathbb{R} and Ψ^- being concave, and let $P = P^+ + P^-$ be a similar splitting that is convex/concave on a suitable superset of $[-1, 1]$, where we recall that φ need not remain in $[-1, 1]$ for the quartic potential (3.3). We also define $\varrho^\pm := (P^\pm)'$. For the schemes PF^{obs}-FEM and PF^{qua}-FEM we set $\Psi^-(s) = -\frac{1}{2} s^2$ and

$$(i) \varrho^+(s) = 0, \quad (ii) \varrho^+(s) = 0, \quad (iii) \varrho^+(s) = \frac{3}{2} s, \quad (iv) \varrho^+(s) = 2 s$$

for the choices of ϱ in (3.8). The semi-implicit time discretization employed by the schemes PF^{obs}-FEM and PF^{qua}-FEM can then be formulated as:

$$\vartheta (w_n - w_{n-1}) + \lambda (\varrho^+(\varphi_n) + \varrho^-(\varphi_{n-1})) (\varphi_n - \varphi_{n-1}) - \tau \nabla \cdot (b(\varphi_{n-1}) \nabla w_n) = 0, \quad (3.19a)$$

$$c_\Psi \frac{a}{\alpha} (\varrho^+(\varphi_n) + \varrho^-(\varphi_{n-1})) w_n = \varepsilon \frac{\rho}{\alpha} \frac{\varphi_n - \varphi_{n-1}}{\tau} - \varepsilon \Delta \varphi_n + \varepsilon^{-1} ((\Psi^+)')(\varphi_n) + (\Psi^-)'(\varphi_{n-1}). \quad (3.19b)$$

With this time discretization existence of a unique solution (φ_n^h, w_n^h) to the fully discrete scheme can be shown for arbitrary time step sizes τ if $\varrho^+ = 0$, where w_n^h may not be unique if $\vartheta = 0$ and $\partial_N \Omega = \partial \Omega$ in very rare circumstances. Moreover, any solution to the semi-implicit schemes PF^{obs}-FEM and PF^{qua}-FEM is stable; see [16] for details. The semi-implicit time discretization in (3.19a,b) can be modified to an implicit time discretization by replacing (3.19b) with

$$c_\Psi \frac{a}{\alpha} (\varrho^+(\varphi_n) + \varrho^-(\varphi_{n-1})) w_n = \varepsilon \frac{\rho}{\alpha} \frac{\varphi_n - \varphi_{n-1}}{\tau} - \varepsilon \Delta \varphi_n + \varepsilon^{-1} \Psi'(\varphi_n), \quad (3.20)$$

which then gives rise to a time step size constraint of the form

$$\tau < \rho \alpha^{-1} \varepsilon^2 \quad \text{if } \rho > 0, \quad (3.21)$$

in order to ensure the existence of a unique, stable solution in the case $\varrho^+ = 0$ and $\rho > 0$. In the situation $\vartheta = \rho = 0$ and $\varrho(s) = \frac{1}{2}$, with $\partial_N \Omega = \partial \Omega$, which has been treated by the present authors in [15], a stronger time step constraint of the form $\tau = \mathcal{O}(\varepsilon^3)$ arises for the implicit discretization (3.20); see also [22, 20]. Here we recall that it is often observed that implicit time discretizations of Allen–Cahn and Cahn–Hilliard type equations yield a better accuracy in time compared to semi-implicit time discretizations as in (3.19a,b); see e.g. [20, 21, 47]. We will present several computations for a variant of PF^{qua}-FEM with the implicit time discretization (3.19a), (3.20) in Sections 4 and 5.

Finally, fully explicit approximations, as advanced in e.g. [63, 46, 62], can also be considered. Here we replace (3.19a,b) by

$$\vartheta (w_n - w_{n-1}) + \lambda \varrho(\varphi_{n-1}) (\varphi_n - \varphi_{n-1}) - \tau \nabla \cdot (b(\varphi_{n-1}) \nabla w_{n-1}) = 0, \quad (3.22a)$$

$$c_\Psi \frac{a}{\alpha} \varrho(\varphi_{n-1}) w_{n-1} = \varepsilon \frac{\rho}{\alpha} \frac{\varphi_n - \varphi_{n-1}}{\tau} - \varepsilon \Delta \varphi_{n-1} + \varepsilon^{-1} ((\Psi^+)')(\varphi_n) + (\Psi^-)'(\varphi_{n-1}). \quad (3.22b)$$

If $\vartheta > 0$ and $\rho > 0$, then the above fully explicit time discretization is well-defined, and in this case stability of the fully discrete scheme can be shown if

$$\tau = \mathcal{O}(h^2). \quad (3.23)$$

In particular, in the case of the obstacle potential (3.4), if $\tau \leq \frac{1}{2} \vartheta \varepsilon \rho (\lambda^2 \alpha)^{-1} \varrho_{\max}^{-2}$, then the solutions to the fully discrete variant of (3.22a,b) are stable if

$$\tau h^{-2} \leq C_\star \min\{\frac{1}{2} \vartheta \mathcal{K}_{\max}^{-1}, \rho \alpha^{-1}\}, \quad (3.24)$$

where $\varrho_{\max} := \max_{s \in [-1,1]} |\varrho(s)|$, $\mathcal{K}_{\max} := \max\{\mathcal{K}_+, \mathcal{K}_-\}$ and where C_\star is a constant only depending on the spatial mesh. The advantage of (3.22a,b) over (3.19a,b) is that the discretized systems of equations now decouple in space, which leads to huge efficiency gains when the computations are performed in parallel on a large cluster. However, in practice this advantage is often negated because (3.23), together with e.g. (3.17), enforces that very small time steps need to be taken. In Section 4.2 and in Section 5 we will present computations for a variant of PF^{obs}-FEM with an explicit time discretization as in (3.22a,b).

4 Quantitative comparison for isotropic problems

A standard validation used for phase field models in the literature is the comparison of tip velocities between the computed phase field discretizations and real world measurements from the laboratory, see e.g. [52, 67]. Here the physical parameters in the phase field model have to be chosen appropriately, so that they correspond to the physical properties of the material in question. However, often the exact values of these parameters are unknown or

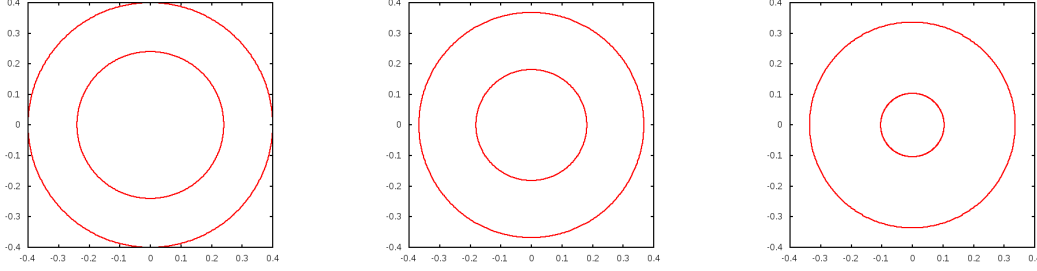


Figure 1: The true solution from (4.2a) at times $t = 0, 10^{-3}, 2 \times 10^{-3}$.

they are themselves based on measurements. Here we propose a much simpler quantitative validation, which makes use of known radially symmetric solutions to the underlying sharp interface problem in the isotropic case. We would argue that such a simple comparison should be part of the validation of every phase field method to be proposed in the literature. It gives an indication of the accuracy of the overall method and it helps to fine-tune the discretization parameters that should be used for the anisotropic physical applications.

In particular, in this section we consider the following isotropic variant of (2.3a–e). Find $u : \Omega \times [0, T] \rightarrow \mathbb{R}$ and the interface $(\Gamma(t))_{t \in [0, T]}$ such that for all $t \in (0, T]$ it holds that:

$$\vartheta u_t - \Delta u = f \quad \text{in } \Omega \setminus \Gamma(t), \quad (4.1a)$$

$$\left[\frac{\partial u}{\partial \mathbf{n}} \right]_{\Gamma(t)} = -\mathcal{V} \quad \text{on } \Gamma(t), \quad (4.1b)$$

$$\rho \mathcal{V} = \alpha \kappa - u \quad \text{on } \Gamma(t), \quad (4.1c)$$

$$\frac{\partial u}{\partial \nu} = 0 \quad \text{on } \partial_N \Omega, \quad u = u_D \quad \text{on } \partial_D \Omega, \quad (4.1d)$$

$$\Gamma(0) = \Gamma_0, \quad \vartheta u(\cdot, 0) = \vartheta u_0 \quad \text{in } \Omega. \quad (4.1e)$$

Here $f : [0, T] \rightarrow \mathbb{R}$ in (4.1a) is a given spatially homogeneous forcing term. In the phase field approximation (3.5a–d), (3.6a–c) this forcing appears analogously as a right hand side term f in (3.5a). Note that for $f = 0$ the above system (4.1a–e) corresponds to (2.3a–e) with (2.2), (2.4) and $\mathcal{K}_\pm = a = \lambda = 1$.

4.1 Mullins–Sekerka problem

We first consider the quasi-static case $\vartheta = \rho = 0$. To this end we take the known solution of an annular region $\Omega_-(t)$, for which the inner boundary shrinks to a point so that $\Omega_-(t)$ becomes a disk for sufficiently large t . Here we take $\alpha = 1$ and let $\partial_N \Omega = \partial \Omega$. In addition, $\Gamma(0) = \Gamma_0$ consists of two concentric circles/spheres. It is then not difficult to show that the two radii $r_1 < r_2$ satisfy the following system of nonlinear ODEs: In the case $d = 2$ we have

$$[r_1]_t = -\frac{1}{r_1} \frac{\frac{1}{r_1} + \frac{1}{r_2}}{\ln \frac{r_2}{r_1}} \quad \text{and} \quad [r_2]_t = -\frac{1}{r_2} \frac{\frac{1}{r_1} + \frac{1}{r_2}}{\ln \frac{r_2}{r_1}} = \frac{r_1}{r_2} [r_1]_t \quad \forall t \in [0, T_0), \quad (4.2a)$$

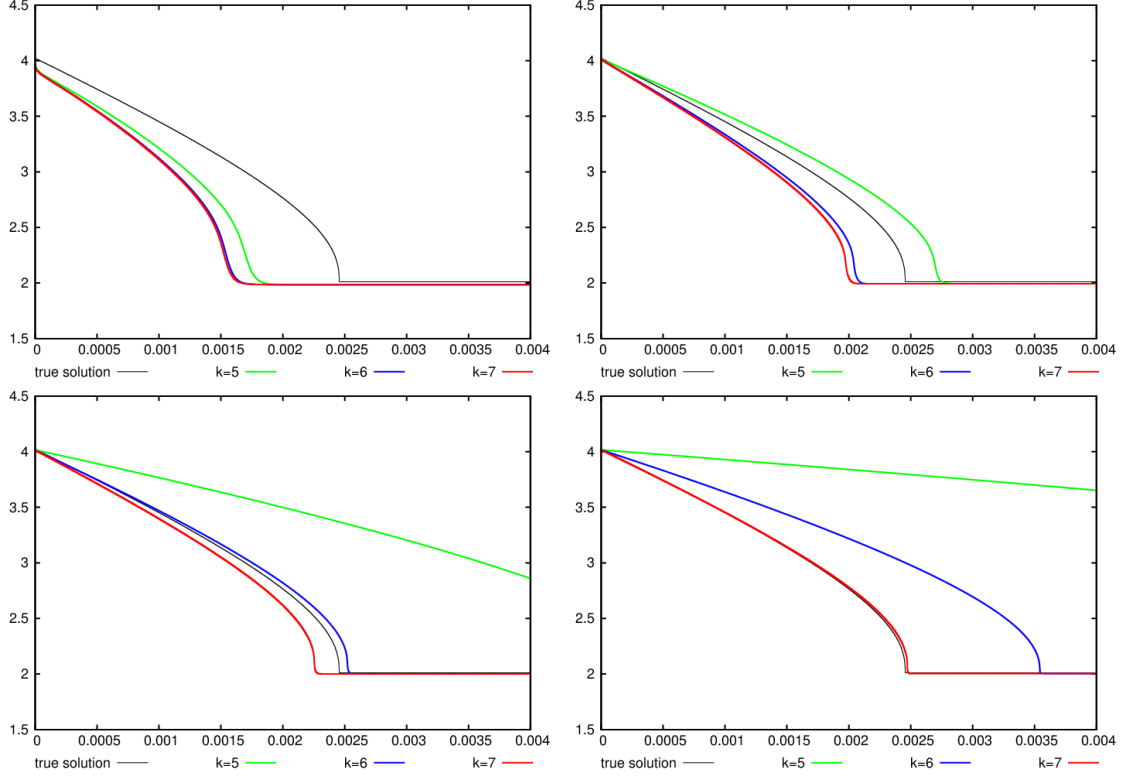


Figure 2: (PF_(i)^{qua}-FEM, $\varepsilon^{-1} = 8\pi, 16\pi, 32\pi, 64\pi$) Comparison of the energies \mathcal{F} and $\mathcal{F}_\varepsilon^h$ for the benchmark problem 1 with $T = 4 \times 10^{-3}$. The uniform time step sizes are chosen as $\tau = 10^{-k}$, $k = 5 \rightarrow 7$.

while for $d = 3$ it holds that

$$[r_1]_t = -\frac{2}{r_1^2} \frac{r_1 + r_2}{r_2 - r_1} \quad \text{and} \quad [r_2]_t = -\frac{2}{r_2^2} \frac{r_1 + r_2}{r_2 - r_1} = \frac{r_1^2}{r_2^2} [r_1]_t \quad \forall t \in [0, T_0), \quad (4.2b)$$

where T_0 is the extinction time of the smaller sphere, i.e. $\lim_{t \rightarrow T_0} r_1(t) = 0$, see e.g. [18, 76]. Note that the corresponding solution u satisfying (2.3a–e) is given by the radially symmetric function

$$u(x, t) = \begin{cases} -\frac{d-1}{r_2(t)} & |x| \geq r_2(t), \\ \begin{cases} \frac{1}{r_1(t)} - \ln \frac{|x|}{r_1(t)} \frac{\frac{1}{r_1(t)} + \frac{1}{r_2(t)}}{\ln \frac{r_2(t)}{r_1(t)}} & d = 2 \\ -\frac{4}{r_2(t)-r_1(t)} + \frac{2}{|x|} \frac{r_1(t)+r_2(t)}{r_2(t)-r_1(t)} & d = 3 \end{cases} & r_1(t) \leq |x| \leq r_2(t), \\ \frac{d-1}{r_1(t)} & |x| \leq r_1(t). \end{cases} \quad (4.3)$$

As (4.2a,b) does not appear to be analytically solvable, it needs to be integrated numerically to compute the solution $(r_1, r_2)(t)$, for $t \in [0, T]$, where $T < T_0$. Possible strategies to integrate (4.2a,b) to a high accuracy are described in [12]. We visualize the evolution of $\Gamma(t)$ over the time interval $[0, 2 \times 10^{-3}]$ in Figure 1. The above true solution forms the basis

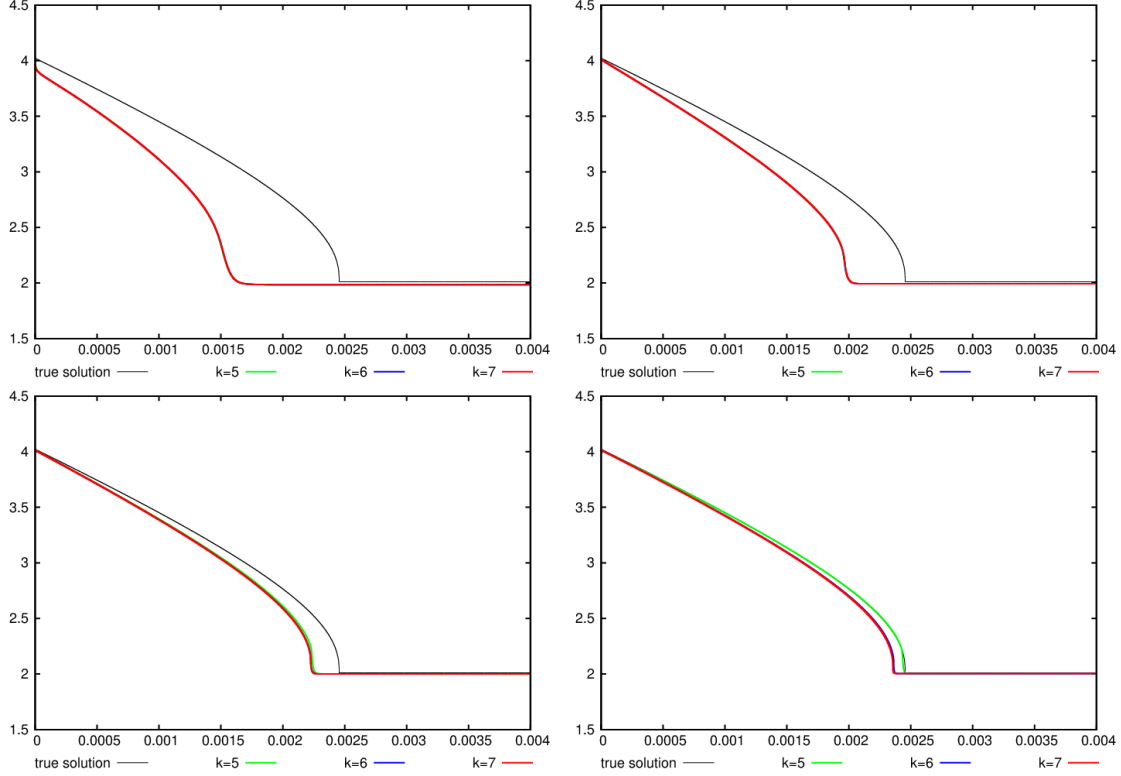


Figure 3: (PF_(i)^{qua}-FEM with the implicit time discretization from (3.20), $\varepsilon^{-1} = 8\pi, 16\pi, 32\pi, 64\pi$) Comparison of the energies \mathcal{F} and $\mathcal{F}_\varepsilon^h$ for the benchmark problem 1 with $T = 4 \times 10^{-3}$. The uniform time step sizes are chosen as $\tau = 10^{-k}$, $k = 5 \rightarrow 7$.

of our first benchmark problem:

Benchmark problem 1: 2d Mullins–Sekerka with $\vartheta = \rho = 0$.

True solution (4.2a), (4.3) to (4.1a–e) with $\vartheta = \rho = 0$ and $\alpha = 1$.

Initial data $(r_1, r_2)(0) = (0.24, 0.4)$.

Domain $\Omega = (-\frac{1}{2}, \frac{1}{2})^2$ with $\partial_N \Omega = \partial \Omega$.

Time interval $[0, T]$ with $T = 10^{-3}$ so that $(r_1, r_2)(T) \approx (0.18, 0.37)$.

In Figure 2 we compare the energy \mathcal{F} of the true sharp interface solution, recall (2.6), to the corresponding energies $\mathcal{F}_\varepsilon^h \approx \mathcal{F}_\varepsilon$, recall (3.13), of the finite element approximations from the algorithm PF_(i)^{qua}-FEM on the time interval $[0, 4 \times 10^{-3}]$. Here we recall that for the given data and the given evolution it holds that

$$\mathcal{F}(\Gamma, u) = |\Gamma(t)| := \int_{\Gamma(t)} 1 \, ds = 2\pi (r_1(t) + r_2(t)).$$

Very similar energy plots can be obtained for the other variants of PF_(i)^{qua}-FEM and those of PF_(i)^{obs}-FEM. We note that for decreasing ε , the time step size τ needs to be chosen smaller and smaller in order to capture the correct time scaling of the evolution. We compare this computation for PF_(i)^{qua}-FEM, which uses a semi-implicit discretization in time, now with one computation for the implicit time discretization as in (3.20). Here we recall that better

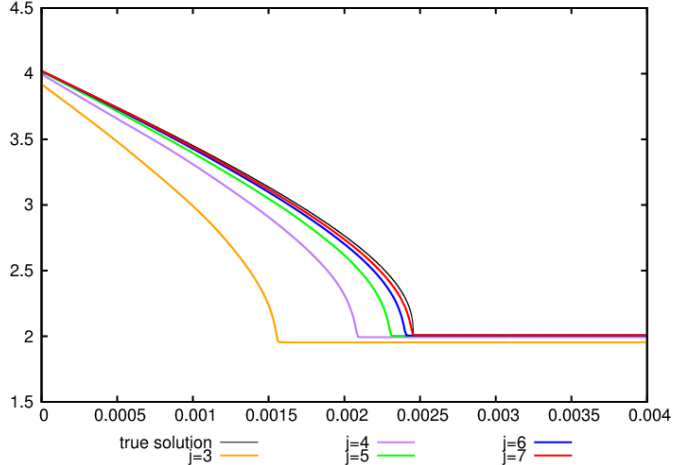


Figure 4: (PFEM) Comparison of the energies \mathcal{F} and \mathcal{F}^h for the benchmark problem 1 with $T = 4 \times 10^{-3}$. The uniform time step size is chosen as $\tau = 10^{-5}$, while the spatial discretizations are proportional to 2^{-j} , $j = 3 \rightarrow 7$.

accuracy for such discretizations has been reported in [20] for the isotropic Cahn–Hilliard equation, i.e. (3.5a), (3.6a) for (2.2) with (3.4), (3.8)(i) and with $\vartheta = \rho = 0$. In fact, here we observe a similar behaviour. See Figure 3, where even for very large choices of τ the time evolution of the phase field model seems to be captured accurately. Finally, we show some discrete energies $\mathcal{F}^h \approx \mathcal{F}$ from the parametric scheme PFEM in Figure 4. Here we choose rather crude discretization parameters, since otherwise the discrete energies \mathcal{F}^h would lie virtually on top of the true energy \mathcal{F} .

In Table 1 we present the errors in r_1 and in u for the scheme PF_(i)^{obs}-FEM for a selection of interface parameters ε and for a range of discretization parameters h_f and τ for the benchmark problem 1. The displayed error quantities are defined as $\|w^h - u\|_{L^2} := (\tau \sum_{0 \leq n \leq T/\tau} \|w^h(\cdot, n\tau) - u(\cdot, n\tau)\|_{L^2(\Omega)}^2)^{\frac{1}{2}}$ and $\|r_{x_1}^h - r_1\|_{L^\infty} := \max_{0 \leq n \leq T/\tau} |r_{x_1}^h(n\tau) - r_1(n\tau)|$, where $r_{x_1}^h(t) := \inf\{s \geq 0 : \varphi^h(s e_1, t) = 0\}$, with $e_1 = (1, 0)^T$ being the first unit vector in \mathbb{R}^2 , denotes the phase field approximation of the inner radius. We also show the number of degrees of freedom (DOFs) for the calculation of the discrete solution for the final time step at time $t = T$. The presented overall CPU times are for a single-thread computation on an Intel i7-860 (2.8 GHz) processor with 8 GB of main memory. For the benchmark problem 1 the remaining variants of PF^{obs}-FEM and PF^{qua}-FEM exhibit very similar errors to the ones in Table 1, and so we do not present them here. In later computations we will also employ the stronger norm $\|w^h - u\|_{L^\infty} := \max_{0 \leq n \leq T/\tau} \|w^h(\cdot, n\tau) - u(\cdot, n\tau)\|_{L^\infty(\Omega)}$ for the temperature error. However, for the experiments in Table 1 no convergence can be observed in the $L^\infty(\Omega_T)$ -error for the true temperature (4.3) for the phase field approximations. In fact, for the computations in Table 1 the errors $\|w^h - u\|_{L^\infty}$ are in the interval $[1, 16]$, where we note that the true solution (4.3) itself remains in the range $[-2.8, 5.6]$ over the computed time interval. It is for this reason that we report the weaker error norms $\|w^h - u\|_{L^2}$ in Table 1.

A repeat of the computation in Table 1, but now for an implicit time discretization of

ε^{-1}	$2^{\frac{1}{2}}/h_f$	τ	$\ r_{x_1}^h - r_1\ _{L^\infty}$	$\ w^h - u\ _{L^2}$	DOFs(T)	CPU time
8π	64	10^{-5}	1.3004e-02	1.8448e-03	4522	5 secs
	64	10^{-6}	1.3154e-02	9.9918e-04	4402	39 secs
	64	10^{-7}	1.3175e-02	3.2861e-04	4354	6:54 mins
	128	10^{-7}	1.4283e-02	3.5051e-04	15626	37:22 mins
16π	128	10^{-5}	1.4139e-02	2.1678e-03	10378	15 secs
	128	10^{-6}	2.6476e-03	2.5879e-04	10130	1:58 mins
	128	10^{-7}	4.9843e-03	1.0553e-04	10106	17:06 mins
	256	10^{-7}	5.5154e-03	1.1024e-04	34682	1:23 hours
32π	256	10^{-5}	3.4984e-02	5.6999e-03	23362	50 secs
	256	10^{-6}	6.2022e-03	3.4521e-04	21650	6:28 mins
	256	10^{-7}	8.8958e-04	3.7115e-05	21082	50:03 mins
	512	10^{-7}	1.8543e-03	3.3740e-05	74322	5:04 hours
64π	512	10^{-5}	5.0345e-02	8.2731e-03	52602	1:54 mins
	512	10^{-6}	2.2346e-02	1.2118e-03	49370	17:19 mins
	512	10^{-7}	4.7000e-03	1.1020e-04	46922	2:14 hours
	1024	10^{-7}	2.1723e-03	3.5938e-05	166498	15:50 hours
128π	1024	10^{-5}	5.6324e-02	9.1597e-03	122314	7:25 mins
	1024	10^{-6}	4.2515e-02	2.2390e-03	118818	1:01 hours
	1024	10^{-7}	1.5232e-02	2.8138e-04	112794	9:50 hours
	2048	10^{-7}	1.0919e-02	1.8112e-04	404962	68:23 hours

Table 1: Benchmark problem 1 for PF_(i)^{obs}-FEM.

PF_(i)^{qua}-FEM can be seen in Table 2. One clearly observes that, for fixed ε , the errors $\|r_{x_1}^h - r_1\|_{L^\infty}$ and $\|w^h - u\|_{L^2}$ soon appear to be almost independent of the time step size τ . This indicates that the implicit time discretization from (3.20) manages to eliminate the temporal discretization error relatively quicker than the semi-implicit discretization from (3.19a,b). Moreover, for small ε and fixed τ , the error in the approximation of the sharp interface problem (4.1a–e) is in general significantly smaller for the implicit time discretization. We remark that the converged errors in Table 2 appear to indicate a convergence of $\mathcal{O}(\varepsilon)$ in the error $\|r_{x_1}^h - r_1\|_{L^\infty}$, with a similar convergence rate for the error $\|w^h - u\|_{L^2}$, if discretization errors are neglected.

Finally we note that the numbers in Tables 1 and 2 indicate that refining the mesh discretization parameters h_f , and hence h_c , in general does not reduce the error. Hence choosing $h_c = 8h_f = \pi\varepsilon$ appears to be sufficient for classical phase field model computations, and we will restrict ourselves to this choice from now on in this paper.

We compare these convergence experiments with the corresponding errors for the sharp interface algorithm PFEM in Table 3. For these sets of experiments we always choose $h_\Gamma \approx h_f$. Here the error quantities $\|u^h - u\|_{L^\infty}$ and $\|u^h - u\|_{L^2}$ are defined as $\|w^h - u\|_{L^\infty}$

ε^{-1}	$2^{\frac{1}{2}}/h_f$	τ	$\ r_{x_1}^h - r_1\ _{L^\infty}$	$\ w^h - u\ _{L^2}$	DOFs(T)	CPU time
8π	64	10^{-5}	3.5385e-02	7.8725e-03	5018	10 secs
	64	10^{-6}	3.5228e-02	2.4832e-03	5018	1:06 mins
	64	10^{-7}	3.5211e-02	7.8429e-04	5018	12:30 mins
	128	10^{-7}	3.6235e-02	7.9552e-04	18658	50:07 mins
16π	128	10^{-5}	1.4453e-02	2.2343e-03	11514	22 secs
	128	10^{-6}	1.4667e-02	7.2292e-04	11530	2:20 mins
	128	10^{-7}	1.4675e-02	2.2894e-04	11514	27:29 mins
	256	10^{-7}	1.5018e-02	2.3527e-04	38858	1:31 hours
32π	256	10^{-5}	5.6651e-03	8.2274e-04	24802	58 secs
	256	10^{-6}	6.4112e-03	2.9604e-04	24290	7:23 mins
	256	10^{-7}	6.4838e-03	9.6155e-05	24322	1:06 hours
	512	10^{-7}	6.6777e-03	1.0156e-04	83690	5:41 hours
64π	512	10^{-5}	3.1282e-04	1.3540e-04	54298	2:20 mins
	512	10^{-6}	2.5224e-03	1.1540e-04	53466	17:31 mins
	512	10^{-7}	2.8135e-03	4.4061e-05	53114	3:27 hours
	1024	10^{-7}	3.0098e-03	4.2577e-05	185410	20:03 hours
128π	1024	10^{-5}	8.3850e-03	1.4662e-03	128866	15:56 mins
	1024	10^{-6}	3.3622e-04	2.2218e-05	123770	1:17 hours
	1024	10^{-7}	8.3440e-04	1.5965e-05	123402	10:46 hours
	2048	10^{-7}	1.1768e-03	1.6903e-05	437330	116:48 hours

Table 2: Benchmark problem 1 for PF_(i)^{qua}-FEM with the implicit time discretization from (3.20).

and $\|w^h - u\|_{L^2}$ as before, but with w^h replaced by u^h . In addition, we let $\|r_1^h - r_1\|_{L^\infty} := \max_{0 \leq n \leq T/\tau} \max_{p \in \Gamma_1^h(n\tau)} \|p - r_1(n\tau)\|$, with $\Gamma_1^h(t)$ denoting the parametric approximation of the inner circle of the true solution $\Gamma(t)$. Note that the norm in the definition of $\|r_1^h - r_1\|_{L^\infty}$ employed here is much stronger than the phase field equivalent $\|r_{x_1}^h - r_1\|_{L^\infty}$ introduced earlier, where the difference between the true interface position $r_1(t)$ and the phase field approximation is measured in the x_1 -coordinate direction only. All of the error quantities shown in Table 3 appear to be converging with order at least $\mathcal{O}(h)$ if the time discretization errors are neglected.

The numbers in Tables 1–3 convey a very clear message. Firstly, we recall that the experiments in Tables 1 and 2 do not converge in the norm $\|w^h - u\|_{L^\infty}$, whereas $\|u^h - u\|_{L^\infty}$ in Table 3 does appear to converge with $\mathcal{O}(h)$. Secondly, we can see that even with computations that take almost 5 days, the phase field schemes PF_(i)^{obs}-FEM and PF_(i)^{qua}-FEM cannot reduce the error in the radius to below 3×10^{-4} . Yet, better accuracies for the radius can be achieved with the sharp interface approximation PFEM, running on the same computing hardware, in less than a minute. Hence, for this measurement, the simulations with PFEM are at least 7 000 times faster than the computations with PF_(i)^{obs}-FEM and

$2^{\frac{1}{2}}/h_f$	τ	$\ r_1^h - r_1\ _{L^\infty}$	$\ u^h - u\ _{L^\infty}$	$\ u^h - u\ _{L^2}$	DOFs(T)	CPU time
8	10^{-4}	3.6782e-02	2.8260e-00	3.5916e-02	113	0 secs
8	10^{-5}	4.2433e-02	4.8862e-00	4.1925e-02	113	0 secs
16	10^{-4}	1.1028e-02	9.5419e-01	1.2123e-02	285	0 secs
16	10^{-5}	1.3394e-02	1.7413e-00	1.5531e-02	285	0 secs
32	10^{-4}	3.6288e-03	4.3183e-01	4.8601e-03	693	0 secs
32	10^{-5}	5.7298e-03	6.3045e-01	7.1794e-03	657	1 secs
64	10^{-4}	7.7318e-04	2.9301e-01	2.8734e-03	1585	0 secs
64	10^{-5}	2.4803e-03	2.9384e-01	3.2140e-03	1473	1 secs
128	10^{-4}	5.8266e-04	3.1247e-01	3.2813e-03	3553	0 secs
128	10^{-5}	1.1406e-03	1.1283e-01	1.4618e-03	3213	3 secs
128	10^{-6}	1.3262e-03	1.5152e-01	1.7016e-03	3173	32 secs
256	10^{-4}	1.1384e-03	3.4935e-01	3.6955e-03	8289	1 secs
256	10^{-5}	4.7583e-04	5.9495e-02	6.7789e-04	6945	7 secs
256	10^{-6}	6.4981e-04	7.6398e-02	8.4454e-04	6777	1:11 mins
512	10^{-4}	1.4098e-03	3.6302e-01	3.8770e-03	20381	3 secs
512	10^{-5}	1.3003e-04	3.4588e-02	3.4619e-04	16109	19 secs
512	10^{-6}	2.9886e-04	3.4579e-02	3.9724e-04	15649	3:02 mins
1024	10^{-4}	1.4724e-03	3.6426e-01	3.9180e-03	43133	6 secs
1024	10^{-5}	3.8716e-05	3.1143e-02	3.2082e-04	41757	57 secs
1024	10^{-6}	1.3093e-04	1.4765e-02	1.8090e-04	39493	9:31 mins
2048	10^{-4}	1.5121e-03	3.6991e-01	3.9402e-03	93385	18 secs
2048	10^{-5}	1.1372e-04	3.7037e-02	3.6346e-04	120429	3:35 mins
2048	10^{-6}	5.3291e-05	6.9988e-03	7.7964e-05	112285	32:22 mins

Table 3: Benchmark problem 1 for PFEM.

PF^{qua}-FEM. The main reason behind this very slow convergence appears to be that the biggest contribution to the observed error comes from the interfacial parameter ε . Hence in order to obtain reasonable errors, ε needs to be taken very small, which on recalling (3.17) implies that the discretization parameters need to be chosen very small as well; recall also (3.11). Unfortunately, phase field computations thus soon reach the limit of what is computable on today's computer hardware. As an aside we note that when comparing CPU times between e.g. PF_(i)^{obs}-FEM and PFEM in terms of degrees of freedom, then it is crucial to take into account the value of τ , as this will be indirectly proportional to the number of algebraic systems that need to be solved during the whole simulation. In fact, for the same number of degrees of freedom and the same value of τ , the CPU times between the two different algorithms are similar.

To better visualize the relative performances of PF_(i)^{obs}-FEM in Table 1, PF_(i)^{qua}-FEM in Table 2 and PFEM in Table 3, we present a plot of the errors in the radius r_1 against the

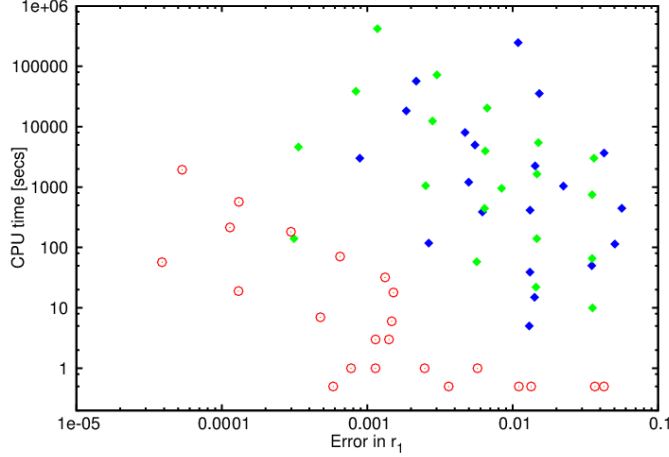


Figure 5: (Benchmark problem 1) Log-log scatter plot of $\|r_{x_1}^h - r_1\|_{L^\infty}$ and $\|r_1^h - r_1\|_{L^\infty}$ against the CPU time for the entries in Table 1 (PF_(i)^{obs}-FEM, blue rhombi), Table 2 (PF_(i)^{qua}-FEM, green rhombi) and Table 3 (PFEM, red circles).

necessary CPU time for all the entries in the three tables in Figure 5. This plot underlines the superiority of the sharp interface algorithm PFEM over the phase field methods.

For the 3d solution (4.2b), (4.3) it is virtually impossible to perform a meaningful convergence experiment for the phase field approximations PF^{obs}-FEM and PF^{qua}-FEM. The reason is that for the same values of ε and for comparable discretization parameters as in e.g. Table 1, the simulations in three space dimensions do not finish in a reasonable amount of time. For an example of a convergence test for the solution (4.2b), (4.3) for the scheme PFEM we refer to [12, Table 6].

4.2 Stefan problem

In this section we consider the full Stefan problem (4.1a-e) with $\vartheta = 1$ and $\rho \geq 0$. Here we adapt the expanding circle/sphere solution introduced in [70, p. 303–304], where the radius of the circle/sphere is given by $r(t)$ with

$$r(t) = (r^2(0) + t)^{\frac{1}{2}}. \quad (4.4a)$$

In particular, we let

$$z(t) = -\frac{\alpha(d-1) + \frac{1}{2}\rho}{r(t)}, \quad v(s) = -\frac{e^{\frac{1}{4}}}{2} \int_1^s \frac{e^{-\frac{1}{4}y^2}}{y^{d-1}} dy.$$

Then it is easy to see that

$$u(x, t) = \begin{cases} z(t) & |x| \leq r(t), \\ z(t) + v\left(\frac{|x|}{r(t)}\right) & |x| > r(t), \end{cases} \quad (4.4b)$$

is the solution to (4.1a–e) with

$$f(t) = \frac{d}{dt}z(t) = \frac{\alpha(d-1) + \frac{1}{2}\rho}{2r^3(t)}, \quad (4.5)$$

and with u_D in (4.1d) replaced by $u|_{\partial_D\Omega}$ on $\partial_D\Omega = \partial\Omega$.

For the Stefan problem with kinetic undercooling we propose the following benchmark problem, where on recalling e.g. (3.16) we note that increasing the parameter $\ell \in \mathbb{N}$ leads to the benchmark problem becoming computationally more and more challenging.

Benchmark problem $2^{(\ell)}$: 2d Stefan problem with $\vartheta = 1$ and $\rho > 0$.

True solution (4.4a,b) to (4.1a–e) with (4.5) and with $\vartheta = 1$ and $\alpha = \rho = 10^{-\ell}$.

Initial data $r(0) = \frac{1}{4}$ and $u_0 = u(\cdot, 0)$ from (4.4b).

Domain $\Omega = (-1, 1)^2$ with $\partial_D\Omega = \partial\Omega$ and $u_D = u|_{\partial_D\Omega}$ from (4.4b).

Time interval $[0, T]$ with $T = \frac{1}{2}$, so that $r(T) = \frac{3}{4}$.

For the benchmark problem $2^{(\ell)}$ with $\ell = 1$, all of the phase field schemes were able to compute the necessary evolutions reasonably well. As an example we show the results for the scheme PF_(iii)^{qua}-FEM in Table 4. Here the definition of $\|r_{x_1}^h - r\|_{L^\infty}$ is the same as $\|r_{x_1}^h - r_1\|_{L^\infty}$ with r_1 replaced by r . In order to be able to assess the absolute temperature errors $\|w^h - u\|_{L^\infty}$, we note that for this benchmark problem the true solution (4.4b) remains in the range $[-0.95, -0.15]$. The same computation now for the implicit time discretization from (3.20) is shown in Table 5. In order to visualize the different behaviour of the two different time discretizations, we plot the scaled phase field approximations $\mathcal{E}_\varepsilon^h \approx \mathcal{E}_\varepsilon$, recall (3.2), together with $|\Gamma(t)| = 2\pi r(t)$ in Figures 6 and 7. Similarly to Section 4.1 it can be seen that the implicit time discretization eliminates the time discretization error in the approximation of the phase field equations sooner than the semi-implicit discretization. Moreover, for the smallest value of ε the absolute errors $\|r_{x_1}^h - r\|_{L^\infty}$ appear to be significantly smaller for the implicit scheme. We remark that the converged errors in Table 5 appear to indicate a convergence of $\mathcal{O}(\varepsilon)$ in the error $\|r_{x_1}^h - r\|_{L^\infty}$, with a similar convergence rate for the error $\|w^h - u\|_{L^2}$, if discretization errors are neglected.

The results for the same benchmark problem for the scheme PF_(ii)^{obs}-FEM with the explicit time discretization from (3.22a,b) are shown in Table 6. Here the reported CPU times are given as guidelines only, because we did not employ any parallelization. Recall that the discrete systems of equations decouple in space, and so a significant speedup of the computations can be expected if they are run in parallel on a large cluster. Firstly, we see that the obtained results appear to confirm the stability constraint (3.24), i.e. $\tau \leq \frac{1}{2}C_\star h^2$. Secondly, it can be observed that once the explicit method is stable, there is hardly any variation in the numerical results when decreasing τ further. And finally, it is clear from Table 6 that there is no convergence in the reported error quantities, i.e. the phase field simulations do not converge to the sharp interface problem (4.1a–e) as $\varepsilon, h_f, \tau \rightarrow 0$. We conjecture that this phenomenon is due to the sensitivity of the explicit method to the employed mesh adaptation strategy, recall Section 3.1. This is confirmed by repeating the simulations for the explicit scheme on uniform grids, see Table 7. Now the errors appear to

ε^{-1}	$2^{\frac{1}{2}}/h_f$	τ	$\ r_{x_1}^h - r\ _{L^\infty}$	$\ w^h - u\ _{L^\infty}$	DOFs(T)	CPU time
4π	32	10^{-2}	2.5442e-01	2.1420e-01	2722	2 secs
	32	10^{-3}	3.0555e-02	3.6722e-02	4082	37 secs
	32	10^{-4}	1.2407e-01	9.6043e-02	4378	4:53 mins
	32	10^{-5}	1.5339e-01	1.3470e-01	4346	47:32 mins
	32	10^{-6}	1.5785e-01	1.3983e-01	4346	13:38 hours
8π	64	10^{-2}	4.1068e-01	2.6415e-01	4082	4 secs
	64	10^{-3}	1.2126e-01	1.1494e-01	7074	3:06 mins
	64	10^{-4}	1.6550e-02	1.5965e-02	8418	32:17 mins
	64	10^{-5}	3.6656e-02	2.7052e-02	8610	3:04 hours
	64	10^{-6}	3.8850e-02	2.8693e-02	8530	22:05 hours
16π	128	10^{-2}	4.7480e-01	2.8186e-01	7786	9 secs
	128	10^{-3}	3.0057e-01	2.1518e-01	11386	1:44 mins
	128	10^{-4}	5.5585e-02	5.2878e-02	16530	35:19 mins
	128	10^{-5}	4.0354e-03	8.8896e-03	17594	4:42 hours
	128	10^{-6}	1.1098e-02	9.9938e-03	18058	37:23 hours
32π	256	10^{-2}	4.9344e-01	2.8715e-01	18970	23 secs
	256	10^{-3}	4.3490e-01	2.6236e-01	21346	6:31 mins
	256	10^{-4}	1.8070e-01	1.4732e-01	31882	1:22 hours
	256	10^{-5}	2.7810e-02	2.6160e-02	38186	13:55 hours
	256	10^{-6}	3.2260e-03	6.0793e-03	39178	93:40 hours

Table 4: Benchmark problem $2^{(\ell)}$ with $\ell = 1$ for PF $_{(iii)}^{\text{qua}}$ -FEM.

be converging, and the absolute errors agree with the corresponding converged errors from the semi-implicit and implicit variants of PF $_{(ii)}^{\text{obs}}$ -FEM, on which we do not report here.

We compare the above phase field errors with the corresponding errors for the sharp interface algorithm PFEM. Here $\|r^h - r\|_{L^\infty}$ is defined as $\|r_1^h - r_1\|_{L^\infty}$, but with Γ_1^h replaced by Γ^h and with r_1 replaced by r . The errors for the benchmark problem $2^{(\ell)}$ with $\ell = 1$ are reported in Table 8. Comparing the results in Tables 4–8 reveals once again that the sharp interface approximations from PFEM are more accurate than the corresponding computations from the phase field schemes PF $^{\text{obs}}$ -FEM and PF $^{\text{qua}}$ -FEM, and they can be obtained in a fraction of the CPU time. For example, we see from the Tables 4, 5 and 8 that in order to reduce the error in both Γ and u below 10^{-2} requires 13 seconds with PFEM, but it takes around 5 and 11 hours, depending on the time discretization, with PF $_{(iii)}^{\text{qua}}$ -FEM. In other words, in this measure the parametric front tracking method PFEM is between 1300 and 2900 times faster than the phase field methods. A visualization of the numerical results in Tables 4–8 can be seen in Figure 10, below.

If we increase the parameter ℓ in the benchmark problem $2^{(\ell)}$ to $\ell = 3$, which on recalling (3.16) means that the problem is now computationally more challenging, then

ε^{-1}	$2^{\frac{1}{2}}/h_f$	τ	$\ r_{x_1}^h - r\ _{L^\infty}$	$\ w^h - u\ _{L^\infty}$	DOFs(T)	CPU time
4π	32	10^{-2}	5.6463e-02	1.4990e-01	3634	5 secs
	32	10^{-3}	1.0972e-01	7.4356e-02	4378	42 secs
	32	10^{-4}	1.5077e-01	1.3089e-01	4394	5:29 mins
	32	10^{-5}	1.5750e-01	1.3943e-01	4346	47:32 mins
	32	10^{-6}	1.5834e-01	1.4032e-01	4346	8:54 hours
8π	64	10^{-2}	1.8482e-01	2.1201e-01	6394	8 secs
	64	10^{-3}	2.0140e-02	3.5234e-02	8498	1:20 mins
	64	10^{-4}	3.7523e-02	2.7306e-02	8578	14:27 mins
	64	10^{-5}	3.8793e-02	2.8669e-02	8530	2:02 hours
	64	10^{-6}	3.9062e-02	2.8841e-02	8530	15:51 hours
16π	128	10^{-2}	3.1725e-01	2.5152e-01	11178	18 secs
	128	10^{-3}	2.4690e-02	6.9721e-02	16954	4:05 mins
	128	10^{-4}	9.0828e-03	1.1014e-02	17698	26:51 mins
	128	10^{-5}	1.1510e-02	1.0304e-02	17898	5:02 hours
	128	10^{-6}	1.1842e-02	1.0627e-02	17826	38:07 hours
32π	256	10^{-2}	4.1167e-01	2.7209e-01	22506	54 secs
	256	10^{-3}	8.5869e-02	1.2716e-01	36050	11:59 mins
	256	10^{-4}	7.0679e-03	1.8667e-02	38938	1:32 hours
	256	10^{-5}	8.7275e-04	5.8758e-03	38906	10:39 hours
	256	10^{-6}	3.5699e-04	5.0530e-03	38922	91:29 hours

Table 5: Benchmark problem $2^{(\ell)}$ with $\ell = 1$ for PF_(iii)^{qua}-FEM with the implicit time discretization from (3.20).

for moderate values of ε all of the phase field schemes exhibit mushy regions in which the phase field approximations φ^h in modulus take on values significantly smaller than unity. This leads to excessive CPU times, since the adaptive mesh strategy uses fine meshes in the interfacial regions. In addition, often the mushy interfacial region quickly reaches the external boundary $\partial\Omega$, which creates additional interfaces, so that the phase field solutions φ^h no longer approximate the radially symmetric sharp interface solution $\Gamma(t)$. Hence in what follows we present convergence experiments for the benchmark problem $2^{(\ell)}$ with $\ell = 3$ only for $\varepsilon^{-1} \geq 16\pi$. See Table 9 for the results for the scheme PF_(ii)^{obs}-FEM, where we note that for this benchmark problem the true solution (4.4b) remains in the range $[-0.35, 0]$. Similar results can be obtained for the other variants of the schemes PF^{obs}-FEM and PF^{qua}-FEM that satisfy $\varrho(1) = 0$, but we omit them here for brevity. In particular, the scheme PF_(ii)^{obs}-FEM with the implicit time discretization from (3.20) yields almost identical results to the ones in Table 9 for the step sizes $\tau = 10^{-k}$, $k = 5 \rightarrow 6$. We remark that for the numbers in Table 9 it is somewhat speculative to infer convergence rates in terms of ε , since the errors $\|r_{x_1}^h - r\|_{L^\infty}$ and $\|w^h - u\|_{L^\infty}$ for the smallest value of ε do not appear to have converged yet in terms of h_f and τ .

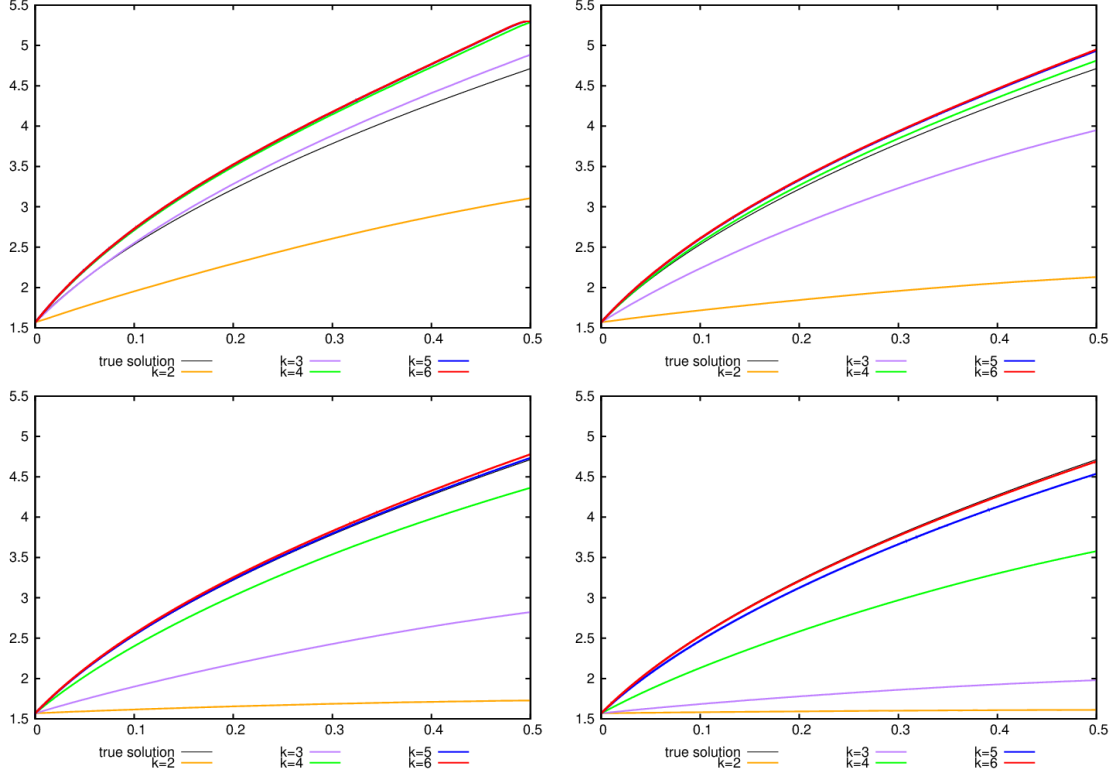


Figure 6: (PF_(iii)^{qua}-FEM, $\varepsilon^{-1} = 4\pi, 8\pi, 16\pi, 32\pi$) Comparison of $|\Gamma(t)|$ and $c_{\Psi}^{-1} \mathcal{E}_{\varepsilon}^h$ for the benchmark problem $2^{(\ell)}$ with $\ell = 1$. The uniform time step sizes are chosen as $\tau = 10^{-k}$, $k = 2 \rightarrow 6$.

We again compare these numbers with the corresponding errors for the sharp interface algorithm PFEM, see Table 10. The results in Tables 9 and 10 confirm once more that the sharp interface approximations from PFEM are more accurate. For example, in order to reduce both the error in Γ and in u to below 10^{-2} requires about a minute with PFEM, but 46 minutes with PF_(ii)^{obs}-FEM. But crucially, it is clear from the numbers in Tables 4, 5 and 9 that only by decreasing ε further can the observed errors for the phase field methods be reduced. This in turn will lead to enforced reductions in h_f and τ , recall e.g. (3.11), (3.17), (3.21) and (3.23). Overall this makes it impossible to perform these computations in practice. On the other hand, the presented errors in Tables 8 and 10 for the scheme PFEM indicate a convergence in the error $\|r^h - r\|_{L^\infty}$ of order at least $\mathcal{O}(h)$, if time discretization effects are neglected. Apart from the run for the finest value of h_f in Table 8, where the time discretization error does not seem to have been eliminated yet, the same can be said about the temperature error $\|u^h - u\|_{L^\infty}$.

In order to visualize the relative performances of PF_(ii)^{obs}-FEM in Table 9 and PFEM in Table 10, we present a plot of the errors in the radius r against the necessary CPU time for all the entries in the two tables in Figure 8.

Similarly to Section 4.1, it is not possible to perform a meaningful convergence test for the solution (4.4a,b) in the case $d = 3$ for the phase field approximations PF_(ii)^{obs}-FEM and

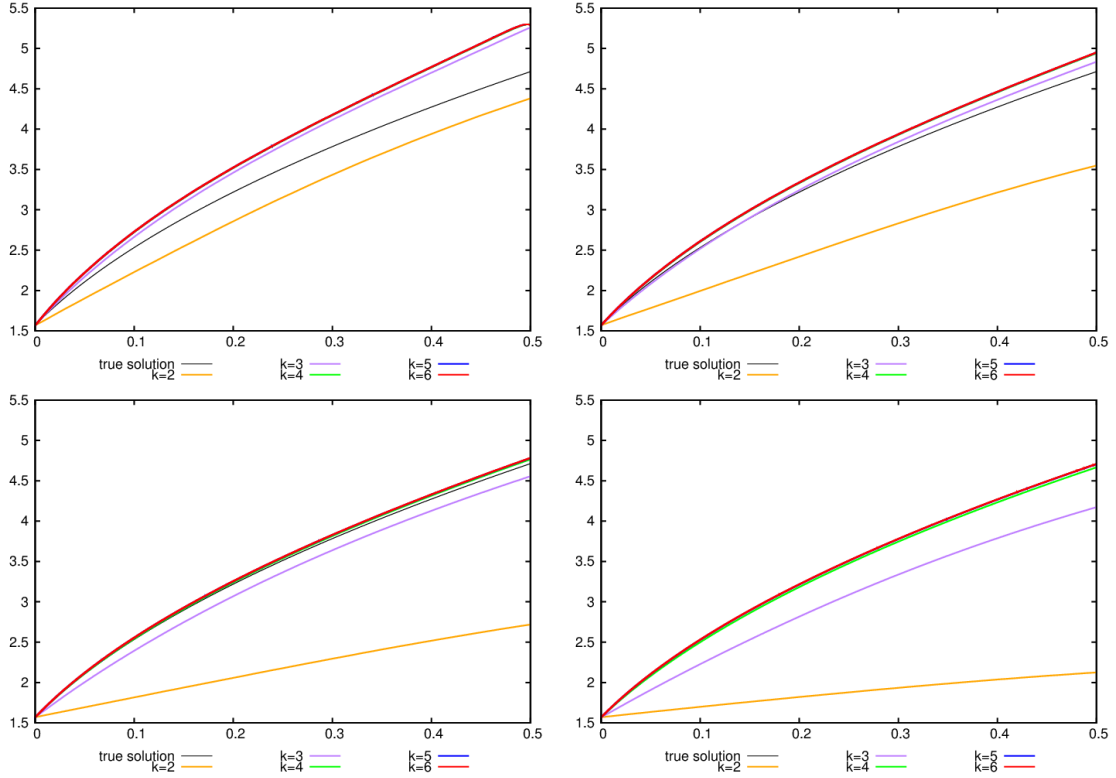


Figure 7: (PF_(iii)^{qua}-FEM with the implicit time discretization from (3.20), $\varepsilon^{-1} = 4\pi, 8\pi, 16\pi, 32\pi$) Comparison of $|\Gamma(t)|$ and $c_{\Psi}^{-1} \mathcal{E}_{\varepsilon}^h$ for the benchmark problem $2^{(\ell)}$ with $\ell = 1$. The uniform time step sizes are chosen as $\tau = 10^{-k}$, $k = 2 \rightarrow 6$.

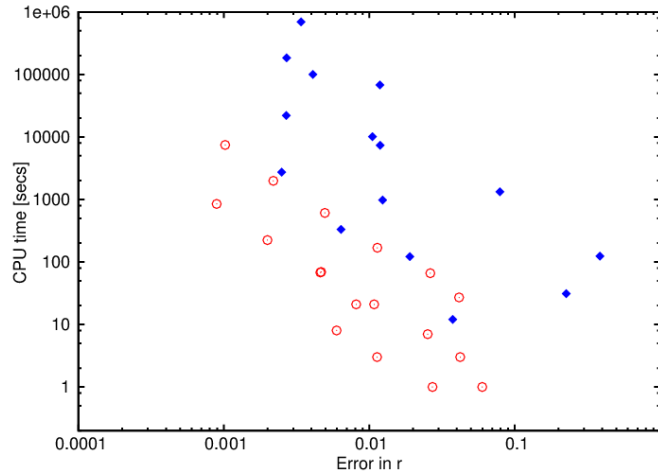


Figure 8: (Benchmark problem $2^{(\ell)}$ with $\ell = 3$) Log-log scatter plot of $\|r_{x_1}^h - r\|_{L^\infty}$ and $\|r^h - r\|_{L^\infty}$ against the CPU time for the entries in Table 9 (PF_(ii)^{obs}-FEM, blue rhombi) and Table 10 (PFEM, red circles).

ε^{-1}	$2^{\frac{1}{2}}/h_f$	τ	$\ r_{x_1}^h - r\ _{L^\infty}$	$\ w^h - u\ _{L^\infty}$	DOFs(T)	CPU time
4π	32	10^{-4}	4.2499e-02	8.9335e-02	3114	1:02 mins
	32	10^{-5}	4.2868e-02	8.9236e-02	3114	10:04 mins
	32	10^{-6}	4.2906e-02	8.9228e-02	3114	1:39 hours
	32	10^{-7}	4.2909e-02	8.9227e-02	3114	16:29 hours
8π	64	10^{-4}	—	—	—	unstable
	64	10^{-5}	2.6258e-02	5.2713e-02	6850	21:47 mins
	64	10^{-6}	2.6311e-02	5.2678e-02	6850	3:19 hours
	64	10^{-7}	2.6317e-02	5.2676e-02	6850	36:27 hours
16π	128	10^{-4}	—	—	—	unstable
	128	10^{-5}	2.4416e-02	3.4926e-02	14706	50:02 mins
	128	10^{-6}	2.4453e-02	3.4777e-02	14706	8:32 hours
	128	10^{-7}	2.4458e-02	3.4767e-02	14706	84:39 hours
32π	256	10^{-4}	—	—	—	unstable
	256	10^{-5}	—	—	—	unstable
	256	10^{-6}	3.6152e-02	3.5620e-02	33074	22:05 hours
	256	10^{-7}	3.6150e-02	3.5595e-02	33138	220:11 hours

Table 6: Benchmark problem $2^{(\ell)}$ with $\ell = 1$ for PF_(ii)^{obs}-FEM with the explicit time discretization from (3.22a,b).

PF^{qua}-FEM. As an example for such a convergence experiment for the parametric scheme PFEM we now consider the three-dimensional analogue of the benchmark problem $2^{(\ell)}$.

Benchmark problem $3^{(\ell)}$: 3d Stefan problem with $\vartheta = 1$ and $\rho > 0$.

Same as benchmark problem $2^{(\ell)}$, but on the domain $\Omega = (-1, 1)^3$.

The corresponding errors are shown in Table 11, where we let $h_\Gamma \approx 6h_f$. Similarly to the two dimensional benchmark problem, the two errors $\|r^h - r\|_{L^\infty}$ and $\|u^h - u\|_{L^\infty}$ appear to converge with order at least $\mathcal{O}(h)$, if time discretization effects are neglected.

Our final benchmark problem is the Stefan problem without interfacial kinetics in the Gibbs–Thomson law. Here we recall from e.g. [52] that often standard, classical phase field methods are not able to deal with this case in practice.

Benchmark problem $4^{(\ell)}$: 2d Stefan problem with $\vartheta = 1$ and $\rho = 0$.

Same as benchmark problem $2^{(\ell)}$, but with $\alpha = 10^{-\ell}$ and $\rho = 0$.

We stress that the approach from [16] for the phase field system has no problems in dealing with the case without interfacial kinetics, i.e. if $\rho = 0$. For example, a computation for the scheme PF_(ii)^{obs}-FEM can be found in Table 12. We compare these results with the corresponding computation for the sharp interface algorithm PFEM in Table 13, where

ε^{-1}	$2^{\frac{1}{2}}/h$	τ	$\ r_{x_1}^h - r\ _{L^\infty}$	$\ w^h - u\ _{L^\infty}$	DOFs(T)	CPU time
4π	32	10^{-5}	4.7109e-02	8.7382e-02	8450	33:11 mins
	32	10^{-6}	4.7154e-02	8.7376e-02	8450	5:32 hours
8π	64	10^{-5}	2.6105e-02	5.0006e-02	33282	3:24 hours
	64	10^{-6}	2.6185e-02	5.0006e-02	33282	32:59 hours
16π	128	10^{-5}	1.7399e-02	3.0422e-02	132098	14:26 hours
	128	10^{-6}	1.7520e-02	3.0420e-02	132098	139:29 hours

Table 7: Benchmark problem $2^{(\ell)}$ with $\ell = 1$ for $\text{PF}_{(ii)}^{\text{obs}}$ -FEM with the explicit time discretization from (3.22a,b) and with a uniform spatial mesh.

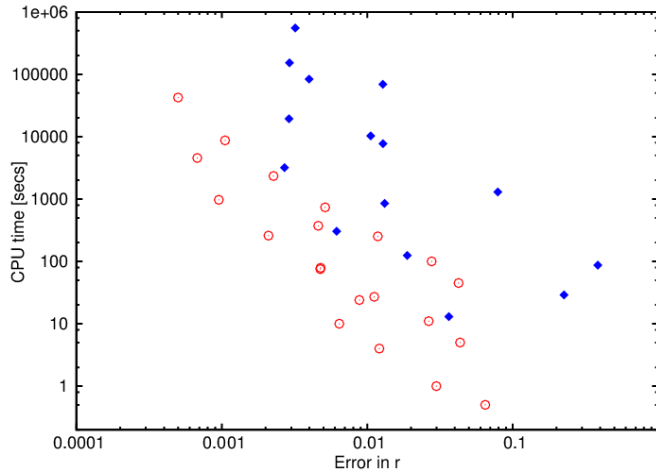


Figure 9: (Benchmark problem $4^{(\ell)}$ with $\ell = 3$) Log-log scatter plot of $\|r_{x_1}^h - r\|_{L^\infty}$ and $\|r^h - r\|_{L^\infty}$ against the CPU time for the entries in Table 12 ($\text{PF}_{(ii)}^{\text{obs}}$ -FEM, blue rhombi) and Table 13 (PFEM, red circles).

once again it appears that the error quantities converge with $\mathcal{O}(h)$ if the time discretization errors are neglected. We visualize the relative performances of $\text{PF}_{(ii)}^{\text{obs}}$ -FEM in Table 12 and PFEM in Table 13 in Figure 9. As before, the performance of PFEM is vastly superior to the corresponding phase field computations.

4.3 Second order accurate isotropic phase field model

In this subsection we recall a variant of the phase field model (3.5a–d), (3.6a–c) which in the isotropic setting (2.2), (2.4) yields a second order convergence in ε to the sharp interface limit; see e.g. [52, 3, 45, 32, 28] for details. In particular, it needs to be assumed that the shape function ϱ , recall (3.7), satisfies (3.9a,b). Clearly, of our examples in (3.8) only the choices (iii) and (iv) satisfy this.

$2^{\frac{1}{2}}/h_f$	τ	$\ r^h - r\ _{L^\infty}$	$\ u^h - u\ _{L^\infty}$	DOFs(T)	CPU time
32	10^{-2}	1.1463e-02	6.1188e-02	1193	0 secs
32	10^{-3}	2.6832e-02	1.9387e-02	1181	3 secs
32	10^{-4}	2.9267e-02	2.1448e-02	1193	23 secs
64	10^{-2}	1.3678e-02	6.3622e-02	2585	0 secs
64	10^{-3}	1.1105e-02	8.4213e-03	2441	5 secs
64	10^{-4}	1.3215e-02	1.2807e-02	2457	52 secs
128	10^{-2}	1.5197e-02	6.4894e-02	6153	1 secs
128	10^{-3}	3.6275e-03	6.6864e-03	5513	13 secs
128	10^{-4}	5.5642e-03	4.9862e-03	5401	2:06 mins
256	10^{-2}	1.7421e-02	6.4862e-02	15497	5 secs
256	10^{-3}	1.0911e-03	6.9236e-03	13157	39 secs
256	10^{-4}	2.2576e-03	1.9430e-03	12941	6:04 mins
512	10^{-2}	1.7903e-02	6.4964e-02	37517	12 secs
512	10^{-3}	1.4352e-03	7.2994e-03	35257	2:12 mins
512	10^{-4}	8.9361e-04	8.3770e-04	34157	20:47 mins
1024	10^{-2}	1.8248e-02	6.5448e-02	89437	45 secs
1024	10^{-3}	1.6084e-03	7.5361e-03	105857	8:56 mins
1024	10^{-4}	3.0915e-04	6.5204e-04	101593	1:23 hours

Table 8: Benchmark problem $2^{(\ell)}$ with $\ell = 1$ for PFEM.

ε^{-1}	$2^{\frac{1}{2}}/h_f$	τ	$\ r_{x_1}^h - r\ _{L^\infty}$	$\ w^h - u\ _{L^\infty}$	DOFs(T)	CPU time
16π	128	10^{-2}	3.7529e-02	1.3113e-01	15098	12 secs
	128	10^{-3}	1.9000e-02	1.7671e-02	15970	2:02 mins
	128	10^{-4}	1.2338e-02	1.5085e-02	15746	16:20 mins
	128	10^{-5}	1.1885e-02	1.4764e-02	15642	2:03 hours
	128	10^{-6}	1.1836e-02	1.4718e-02	15626	18:57 hours
32π	256	10^{-2}	2.2627e-01	2.1834e-01	26306	31 secs
	256	10^{-3}	6.3959e-03	3.5178e-02	34642	5:31 mins
	256	10^{-4}	2.5004e-03	7.2381e-03	34906	45:39 mins
	256	10^{-5}	2.6881e-03	7.6427e-03	34770	6:08 hours
	256	10^{-6}	2.7040e-03	7.6802e-03	34802	51:18 hours
64π	512	10^{-2}	3.8556e-01	2.5703e-01	58226	2:04 mins
	512	10^{-3}	7.9248e-02	1.0625e-01	80330	22:12 mins
	512	10^{-4}	1.0521e-02	1.3930e-02	85218	2:48 hours
	512	10^{-5}	4.1001e-03	5.2299e-03	85714	27:46 hours
	512	10^{-6}	3.3949e-03	6.4424e-03	85842	193:11 hours

Table 9: Benchmark problem $2^{(\ell)}$ with $\ell = 3$ for PF_(ii)^{obs}-FEM.

$2^{\frac{1}{2}}/h_f$	τ	$\ r^h - r\ _{L^\infty}$	$\ u^h - u\ _{L^\infty}$	DOFs(T)	CPU time
32	10^{-2}	5.9808e-02	3.4189e-02	1213	1 secs
32	10^{-3}	4.2215e-02	2.9898e-02	1169	3 secs
32	10^{-4}	4.1433e-02	2.9813e-02	1217	27 secs
64	10^{-2}	2.7229e-02	2.9493e-02	2705	1 secs
64	10^{-3}	2.5199e-02	1.7501e-02	2505	7 secs
64	10^{-4}	2.6297e-02	1.8341e-02	2497	1:06 mins
128	10^{-2}	1.1307e-02	3.0940e-02	6133	3 secs
128	10^{-3}	1.0799e-02	7.7496e-03	5529	21 secs
128	10^{-4}	1.1358e-02	8.4107e-03	5489	2:49 mins
256	10^{-2}	5.9618e-03	3.1694e-02	15781	8 secs
256	10^{-3}	4.6057e-03	3.1840e-03	13165	1:08 mins
256	10^{-4}	4.9513e-03	3.7938e-03	12977	10:08 mins
512	10^{-2}	8.1252e-03	3.2015e-02	37069	21 secs
512	10^{-3}	1.9929e-03	3.5308e-03	35205	3:44 mins
512	10^{-4}	2.1894e-03	1.7126e-03	34149	33:04 mins
1024	10^{-2}	4.6688e-03	3.2259e-02	89301	1:09 mins
1024	10^{-3}	8.9176e-04	3.7858e-03	105993	14:07 mins
1024	10^{-4}	1.0202e-03	7.8635e-04	101517	2:04 hours

Table 10: Benchmark problem $2^{(\ell)}$ for $\ell = 3$ for PFEM.

$2^{\frac{1}{2}}/h_f$	τ	$\ r^h - r\ _{L^\infty}$	$\ u^h - u\ _{L^\infty}$	DOFs(T)	CPU time
32	10^{-2}	1.0373e-01	4.0392e-02	38661	3:06 mins
32	10^{-3}	1.2020e-01	6.0675e-02	38067	23:07 mins
32	10^{-4}	3.4579e-01	1.0935e-01	39826	3:06 hours
64	10^{-2}	2.4115e-02	3.2858e-02	162161	25:31 mins
64	10^{-3}	3.0456e-02	1.9335e-02	147787	2:33 hours
64	10^{-4}	4.7083e-02	2.7765e-02	148036	17:10 hours
128	10^{-2}	1.0819e-02	3.1504e-02	740635	2:08 hours
128	10^{-3}	1.1358e-02	7.7776e-03	603059	12:43 hours
128	10^{-4}	1.6654e-02	1.0916e-02	593187	65:34 hours
256	10^{-2}	8.2692e-03	3.1338e-02	3480836	9:19 hours
256	10^{-3}	5.6216e-03	3.7231e-03	2577960	47:19 hours
256	10^{-4}	6.4224e-03	4.7100e-03	2490788	308:35 hours

Table 11: Benchmark problem $3^{(\ell)}$ with $\ell = 3$ for PFEM.

ε^{-1}	$2^{\frac{1}{2}}/h_f$	τ	$\ r_{x_1}^h - r\ _{L^\infty}$	$\ w^h - u\ _{L^\infty}$	DOFs(T)	CPU time
16 π	128	10^{-2}	3.6341e-02	1.2977e-01	15370	13 secs
	128	10^{-3}	1.8831e-02	1.8600e-02	16226	2:04 mins
	128	10^{-4}	1.3159e-02	1.5797e-02	15818	14:12 mins
	128	10^{-5}	1.2840e-02	1.5560e-02	15890	2:09 hours
	128	10^{-6}	1.2810e-02	1.5510e-02	15890	19:13 hours
32 π	256	10^{-2}	2.2563e-01	2.1820e-01	26362	29 secs
	256	10^{-3}	6.1576e-03	3.4619e-02	34634	5:04 mins
	256	10^{-4}	2.6943e-03	7.5241e-03	34938	53:05 mins
	256	10^{-5}	2.8987e-03	7.9607e-03	34754	5:23 hours
	256	10^{-6}	2.9172e-03	1.1125e-02	34818	42:28 hours
64 π	512	10^{-2}	3.8566e-01	2.5703e-01	58146	1:27 mins
	512	10^{-3}	7.9018e-02	1.0605e-01	80010	21:39 mins
	512	10^{-4}	1.0560e-02	1.3817e-02	85266	2:51 hours
	512	10^{-5}	3.9822e-03	5.3896e-03	86002	23:17 hours
	512	10^{-6}	3.1951e-03	1.0395e-02	86042	154:02 hours

Table 12: Benchmark problem $4^{(\ell)}$ with $\ell = 3$ for PF_(ii)^{obs}-FEM.

From now on we assume that (2.2) and (2.4) hold, and that $\mathcal{K}^+ = \mathcal{K}^- > 0$. Then in place of (3.5a) and (3.6a) we consider

$$\vartheta w_t + \lambda \tilde{\varrho}(\varphi) \varphi_t = \mathcal{K} \Delta w, \quad (4.6a)$$

$$c_\Psi a \alpha^{-1} \varrho(\varphi) w = \varepsilon \alpha^{-1} (\rho + \rho_1 \varepsilon) \varphi_t - \varepsilon \Delta \varphi + \varepsilon^{-1} \Psi'(\varphi), \quad (4.6b)$$

in Ω_T , where $\tilde{\varrho}: \mathbb{R} \rightarrow \mathbb{R}$ is a second shape function that satisfies

$$\tilde{\varrho}(s) \geq 0 \quad \forall s \in [-1, 1], \quad \tilde{\varrho}(s) = \tilde{\varrho}(-s) \quad \forall s \in \mathbb{R}, \quad \int_{-1}^1 \tilde{\varrho}(y) dy = 1.$$

Here ρ_1 in (4.6b) is a correction term that is given by

$$\rho_1 = K \frac{\lambda a}{\mathcal{K}}, \quad (4.7)$$

where, see e.g. [45, Eq. (35)],

$$K := \int_{\mathbb{R}} [1 - P(\Phi(s))] \tilde{P}(\Phi(s)) ds \quad \text{with} \quad \tilde{P}(s) := \int_{-1}^s \tilde{\varrho}(y) dy. \quad (4.8)$$

In (4.8) the function $\Phi: \mathbb{R} \rightarrow \mathbb{R}$ denotes the unique solution to

$$\Phi''(s) - \Psi'(\Phi(s)) = 0 \quad \forall s \in \mathbb{R}, \quad \lim_{s \rightarrow \pm\infty} \Phi(s) = \pm 1, \quad \int_{\mathbb{R}} s \Phi'(s) ds = 0.$$

For the above choices of ϱ , $\tilde{\varrho}$ and ρ_1 , Almgren [3] formally showed second order convergence in the sense that the approximation of the Gibbs–Thomson law is of $\mathcal{O}(\varepsilon^2)$, whereas in [45] it is formally established that

$2^{\frac{1}{2}}/h_f$	τ	$\ r^h - r\ _{L^\infty}$	$\ u^h - u\ _{L^\infty}$	DOFs(T)	CPU time
32	10^{-2}	6.4835e-02	3.5949e-02	1225	0 secs
32	10^{-3}	4.3505e-02	3.0646e-02	1169	5 secs
32	10^{-4}	4.2440e-02	3.0431e-02	1217	45 secs
64	10^{-2}	2.9889e-02	2.9534e-02	2613	1 secs
64	10^{-3}	2.6450e-02	1.8257e-02	2521	11 secs
64	10^{-4}	2.7699e-02	1.9103e-02	2497	1:40 mins
128	10^{-2}	1.2103e-02	3.1028e-02	6109	4 secs
128	10^{-3}	1.1158e-02	8.0117e-03	5529	27 secs
128	10^{-4}	1.1813e-02	8.7200e-03	5489	4:12 mins
256	10^{-2}	6.4202e-03	3.1800e-02	15805	10 secs
256	10^{-3}	4.7724e-03	3.3036e-03	13221	1:19 mins
256	10^{-4}	5.1346e-03	3.9258e-03	13001	12:16 mins
512	10^{-2}	8.8182e-03	3.2129e-02	37161	24 secs
512	10^{-3}	2.0921e-03	3.5487e-03	35117	4:19 mins
512	10^{-4}	2.2635e-03	1.7705e-03	34165	38:59 mins
1024	10^{-2}	4.7558e-03	3.2373e-02	89269	1:15 min
1024	10^{-3}	9.5286e-04	3.8105e-03	105997	16:11 mins
1024	10^{-4}	1.0525e-03	8.1355e-04	101509	2:25 hours
2048	10^{-2}	4.6014e-03	3.2830e-02	295201	6:13 min
2048	10^{-3}	6.7747e-04	3.8557e-03	352153	1:16 hours
2048	10^{-4}	4.9986e-04	3.6634e-04	334785	11:48 hours

Table 13: Benchmark problem $4^{(\ell)}$ for $\ell = 3$ for PFEM.

- the zero level set of the phase field function φ approximates the interface Γ to $\mathcal{O}(\varepsilon^2)$,
- the temperature w in the phase field system approximates the temperature u in the sharp interface problem to $\mathcal{O}(\varepsilon^2)$.

In [32], for the special case $\tilde{\varrho}(s) = \frac{1}{2}$, the above second order approximation results are shown rigorously. In particular, on letting $\mathcal{K} = a = 1$, and on recalling that in their notation $G(s) = c_\Psi P(s)$, it holds that the expression in [32, Eq. (1.6)] for the correction term ρ_1 is given by

$$\begin{aligned} \rho_1 &= \frac{1}{2} \lambda \frac{\int_{\mathbb{R}} [G(1) - G(\Phi(s))](1 + \Phi(s)) \, ds}{\int_{\mathbb{R}} [\Phi'(s)]^2 \, ds} = \frac{1}{2} \lambda c_\Psi \frac{\int_{\mathbb{R}} [1 - P(\Phi(s))](1 + \Phi(s)) \, ds}{\int_{\mathbb{R}} [\Phi'(s)]^2 \, ds} \\ &= \frac{1}{2} \lambda \int_{\mathbb{R}} [1 - P(\Phi(s))](1 + \Phi(s)) \, ds = \lambda K, \end{aligned}$$

and so agrees exactly with (4.7). In addition, on assuming the stronger condition

$$\varrho(s) = \frac{1}{c_\Psi} \sqrt{2\Psi(s)} \tag{4.9}$$

in place of (3.9a,b), the authors in [32] also show rigorously that the full phase field converges to second order. More precisely, in this case the first order correction to the phase field function φ is zero. Of course, the specific choice $\tilde{\varrho}(s) = \frac{1}{2}$ for the interpolation function in the equation for the temperature means that the overall phase field system considered in [32] is not thermodynamically consistent. We refer to [3, 32, 45] for the precise statements of these results.

From now on we consider (4.6a,b) in the case that $\tilde{\varrho} = \varrho$, which means that we return to (3.5a), (3.6a) in the isotropic case (2.2), (2.4) with $\mathcal{K}_+ = \mathcal{K}_-$. In particular, the phase field model (4.6a,b) is now thermodynamically consistent, i.e. it satisfies (3.12) with (2.2), (2.4) and $\mathcal{K}_+ = \mathcal{K}_-$. Since now $\tilde{\varrho} = \varrho$, it follows from (4.8) that

$$K = \int_{\mathbb{R}} [1 - P(\Phi(s))] P(\Phi(s)) ds.$$

In the case of the obstacle potential (3.4), so that $\Phi(s) = \sin(s)$ for $|s| \leq \frac{\pi}{2}$ as in (3.18a), we get that

$$K = \int_{-\frac{\pi}{2}}^{\frac{\pi}{2}} [1 - P(\sin(s))] P(\sin(s)) ds.$$

In particular, for the choice (3.8)(iii), when $P(s) = \frac{1}{16} (3s^5 - 10s^3 + 15s + 8)$, we have that

$$K = \frac{4817}{65536} \pi = 2^{-16} 4817 \pi \approx 0.231. \quad (4.10)$$

We refer to Table 14 for computations for the benchmark problem $2^{(\ell)}$ with $\ell = 1$ for the phase field model (4.6a,b) with the correction term (4.7) and (4.10). Here we denote by $\widehat{\text{PF}}_{(\text{iii})}^{\text{obs}}$ -FEM the scheme $\text{PF}_{(\text{iii})}^{\text{obs}}$ -FEM but for the phase field model (3.5a-d), (3.6a-c) with ρ in (3.6a) replaced by (3.10).

The numbers in Table 14 show that eight points across the interface are not enough to see $\mathcal{O}(\varepsilon^2)$ convergence in the errors in practice. Here we recall that a similar conclusion can be drawn from the results reported in [28, Table 1], where a one-dimensional reformulation of a radially symmetric problem in \mathbb{R}^3 is considered. With 16 points across the interface the error $\|r_{x_1}^h - r\|_{L^\infty}$ in Table 14 appears to converge quadratically in ε , while only linear convergence can be seen in the error $\|w^h - u\|_{L^\infty}$. We also note that the errors $\|r_{x_1}^h - r\|_{L^\infty}$ shown in Table 14 are significantly smaller than the corresponding errors in Tables 4 and 5 for the classical phase field model, i.e. for $\rho_1 = 0$, whereas the improvements in the temperature error $\|w^h - u\|_{L^\infty}$ are less pronounced.

In the case of the quartic potential (3.3), so that $\Phi(s) = \tanh(2^{-\frac{1}{2}} s)$ as in (3.18b), we get that

$$K = \sqrt{2} \int_{\mathbb{R}} [1 - P(\tanh(s))] P(\tanh(s)) ds.$$

In particular, for the choice (3.8)(iii) we have that

$$K = \frac{209\sqrt{2}}{840} \approx 0.352,$$

ε^{-1}	$2^{\frac{1}{2}}/h_f$	τ	$\ r_{x_1}^h - r\ _{L^\infty}$	$\ w^h - u\ _{L^\infty}$	DOFs(T)	CPU time
4π	32	10^{-4}	4.3481e-03	2.7780e-02	3394	5:12 mins
	32	10^{-5}	1.9588e-03	2.4734e-02	3442	39:41 mins
	32	10^{-6}	1.9743e-03	2.4425e-02	3474	5:40 hours
	64	10^{-4}	1.5762e-03	2.5180e-02	11922	24:35 mins
	64	10^{-5}	3.9787e-03	2.1853e-02	11906	2:41 hours
	64	10^{-6}	4.5109e-03	2.1533e-02	11970	29:05 hours
$\sqrt{32}\pi$	64	10^{-4}	9.3961e-03	2.3676e-02	8946	19:06 mins
	64	10^{-5}	9.2783e-04	1.7200e-02	9074	2:25 hours
	64	10^{-6}	1.1183e-03	1.6723e-02	9186	19:37 hours
	128	10^{-4}	8.5330e-03	2.2021e-02	32226	1:46 hours
	128	10^{-5}	9.0354e-04	1.6249e-02	32730	13:02 hours
	128	10^{-6}	1.7709e-03	1.5796e-02	32586	104:40 hours
8π	64	10^{-4}	2.3635e-02	2.9991e-02	7074	15:49 mins
	64	10^{-5}	6.8162e-03	1.6316e-02	7042	1:46 hours
	64	10^{-6}	5.0485e-03	1.5149e-02	7066	14:08 hours
	128	10^{-4}	1.9116e-02	2.5065e-02	24266	1:12 hours
	128	10^{-5}	1.9668e-03	1.2975e-02	24746	9:47 hours
	128	10^{-6}	4.8430e-04	1.2136e-02	24874	65:32 hours

Table 14: Benchmark problem $2^{(\ell)}$ with $\ell = 1$ for $\widehat{\text{PF}}_{(\text{iii})}^{\text{obs}}$ -FEM.

while for the choice (3.8)(iv), on noting that $P(s) = \frac{1}{4}(2 + 3s - s^3)$, it holds that

$$K = \frac{19\sqrt{2}}{60} \approx 0.448. \quad (4.11)$$

We refer to Table 15 for computations for the benchmark problem $2^{(\ell)}$ with $\ell = 1$ for the phase field model (4.6a,b) with the correction term (4.7) and (4.11). Here we denote by $\widehat{\text{PF}}_{(\text{iv})}^{\text{qua}}$ -FEM the scheme PF^{qua}-FEM for the phase field model (3.5a–d), (3.6a–c) with ρ in (3.6a) replaced by (3.10), and with ϱ given by (3.8)(iv). A computation for the scheme $\widehat{\text{PF}}_{(\text{iv})}^{\text{qua}}$ -FEM with the implicit time discretization (3.20) yielded very similar error numbers, and so we omit these results here. What can be clearly seen from Table 15 is that once again we have convergence of order at least $\mathcal{O}(\varepsilon^2)$ in $\|r_{x_1}^h - r\|_{L^\infty}$.

In order to visualize the performances of all the considered methods for the benchmark problem $2^{(\ell)}$ with $\ell = 1$, i.e. including the computations in Tables 14 and 15 for the second order accurate phase field model (4.6a,b), we present a log-log plot of the errors in the radius r against the necessary CPU time for all the entries in the appropriate tables in Figure 10. The plot appears to confirm that computations for the phase field model (4.6a,b) are on average more efficient than computations for the standard phase field model, i.e. (4.6a,b) with $\rho_1 = 0$. However, the finer meshes needed for computations for (4.6a,b), recall Table 14, mean that due to CPU time constraints we cannot choose ε as small as in the standard phase

ε^{-1}	$2^{\frac{1}{2}}/h_f$	τ	$\ r_{x_1}^h - r\ _{L^\infty}$	$\ w^h - u\ _{L^\infty}$	DOFs(T)	CPU time
4π	32	10^{-4}	1.1945e-02	4.1523e-02	4066	7:12 mins
	32	10^{-5}	1.7315e-02	3.9842e-02	4090	52:56 mins
	32	10^{-6}	1.7860e-02	3.9682e-02	4082	8:24 hours
	64	10^{-4}	1.1659e-02	4.1790e-02	14090	29:48 mins
	64	10^{-5}	1.7071e-02	3.9883e-02	14130	4:18 hours
	64	10^{-6}	1.7615e-02	3.9686e-02	14210	43:32 hours
$\sqrt{32}\pi$	64	10^{-4}	5.1351e-03	3.2940e-02	10514	18:46 mins
	64	10^{-5}	4.0145e-03	2.9244e-02	10578	2:41 hours
	64	10^{-6}	5.0498e-03	2.8980e-02	10578	25:57 hours
	128	10^{-4}	5.1726e-03	3.2286e-02	37194	1:09 hours
	128	10^{-5}	3.7103e-03	2.9080e-02	37690	10:37 hours
	128	10^{-6}	4.7916e-03	2.8833e-02	37626	109:39 hours
8π	64	10^{-4}	1.9976e-02	3.2507e-02	8082	12:14 mins
	64	10^{-5}	3.4097e-03	2.2891e-02	8242	2:12 hours
	64	10^{-6}	1.4844e-03	2.2330e-02	8306	16:44 hours
	128	10^{-4}	1.9474e-02	3.0950e-02	27826	1:15 hours
	128	10^{-5}	2.9987e-03	2.2277e-02	28298	7:39 hours
	128	10^{-6}	1.0518e-03	2.1768e-02	28234	65:58 hours

Table 15: Benchmark problem $2^{(\ell)}$ with $\ell = 1$ for $\widehat{\text{PF}}_{(\text{iv})}^{\text{qua}}$ -FEM.

field computations. Finally, the plot in Figure 10 once again underlines the superiority of the sharp interface algorithm PFEM over all the phase field methods.

5 Numerical experiments for anisotropic problems

In this section we present numerical simulations for the anisotropic Stefan problem (2.3a–e). Here we always let $\partial_D\Omega = \partial\Omega$ and $\beta = \gamma$, where we recall (3.1). Moreover, we always choose $\lambda = a = 1$ and, unless otherwise stated, we let $\mathcal{K}_\pm = 1$. In order to appreciate the computational challenges involved with the different experiments, we recall from (3.16), (3.17) and (3.11) that for accurate phase field calculations the following implications arise:

$$-u_D \alpha^{-1} \text{ large} \quad \Rightarrow \quad \varepsilon \text{ small} \quad \Rightarrow \quad h_f, \tau \text{ small.}$$

Moreover, we note that for the fully anisotropic situation a formally second order accurate phase field model similarly to Section 4.3 involves a parameter $\rho_1(\nabla\varphi)$ in place of (4.7) that depends on β, γ and on $\nabla\varphi$, see [52, 53]. We stress that these approaches are not well analyzed so far, e.g. in the spirit of [45, 32]. In particular, to our knowledge there are no formal or rigorous results in the literature on the second order convergence of phase field

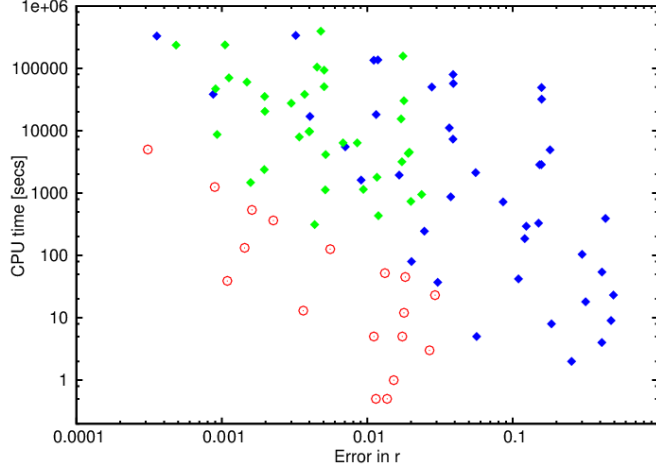


Figure 10: (Benchmark problem $2^{(\ell)}$ with $\ell = 1$) Log-log scatter plot of $\|r_{x_1}^h - r\|_{L^\infty}$ and $\|r^h - r\|_{L^\infty}$ against the CPU time for the entries in Tables 4 and 5 (PF_(iii)^{qua}-FEM, blue rhombi), Tables 14 and 15 ($\widehat{\text{PF}}_{(iii)}^{\text{obs}}$ -FEM and $\widehat{\text{PF}}_{(iv)}^{\text{qua}}$ -FEM, green rhombi) and Table 8 (PFEM, red circles).

models for the fully anisotropic Gibbs–Thomson law. Moreover, our numerical results in the isotropic case showed that the second order models do not give a large gain in computational efficiency. That is why all of our phase field computations in this section are for the standard phase field model (3.5a–d), (3.6a–c).

For the first simulations that we present we choose as anisotropy the regularized l^1 -norm

$$\text{ANI}_1: \quad \gamma(p) = \sum_{j=1}^2 [\delta^2 |p|^2 + p_j^2 (1 - \delta^2)]^{\frac{1}{2}}, \quad \text{with } \delta = 0.3.$$

The radius of the initially circular seed Γ_0 is chosen as 0.1, while we set $\vartheta = 0$, $\alpha = 0.03$ and $\rho = 0.01$. The supercooling at the boundary $\partial_D \Omega = \partial \Omega$ of $\Omega = (-8, 8)^2$ is set to $u_D = -2$.

Three numerical simulations for the scheme PF_(ii)^{obs}-FEM with the interfacial parameter $\varepsilon^{-1} = 4\pi$ can be seen in Figure 11. It can be seen that varying the time discretization parameter τ from 10^{-1} to 10^{-3} has a significant impact on the observed numerical results. However, the observed changes for the smallest value of τ are small, which indicates that the simulation appears to be converging. Very similar results can be obtained for PF_(iii)^{qua}-FEM with the implicit time discretization from (3.20), and so we omit them here.

We compare the above numerical experiments for the phase field method with three simulations for the sharp interface approximation PFEM in Figure 12, where we fix the spatial discretization parameters as $h_\Gamma \approx \frac{1}{2} h_f = \frac{\sqrt{2}}{4}$. Here we observe that even for a very crude time discretization, the evolution is captured remarkably well, and there is very little variation in the numerical results from PFEM when τ is decreased. Also note that it takes (less than) a second of CPU time with PFEM in order to get a good idea about the evolution of the growing crystal, while the phase field methods PF_(iii)^{obs}-FEM and PF_(iii)^{qua}-FEM

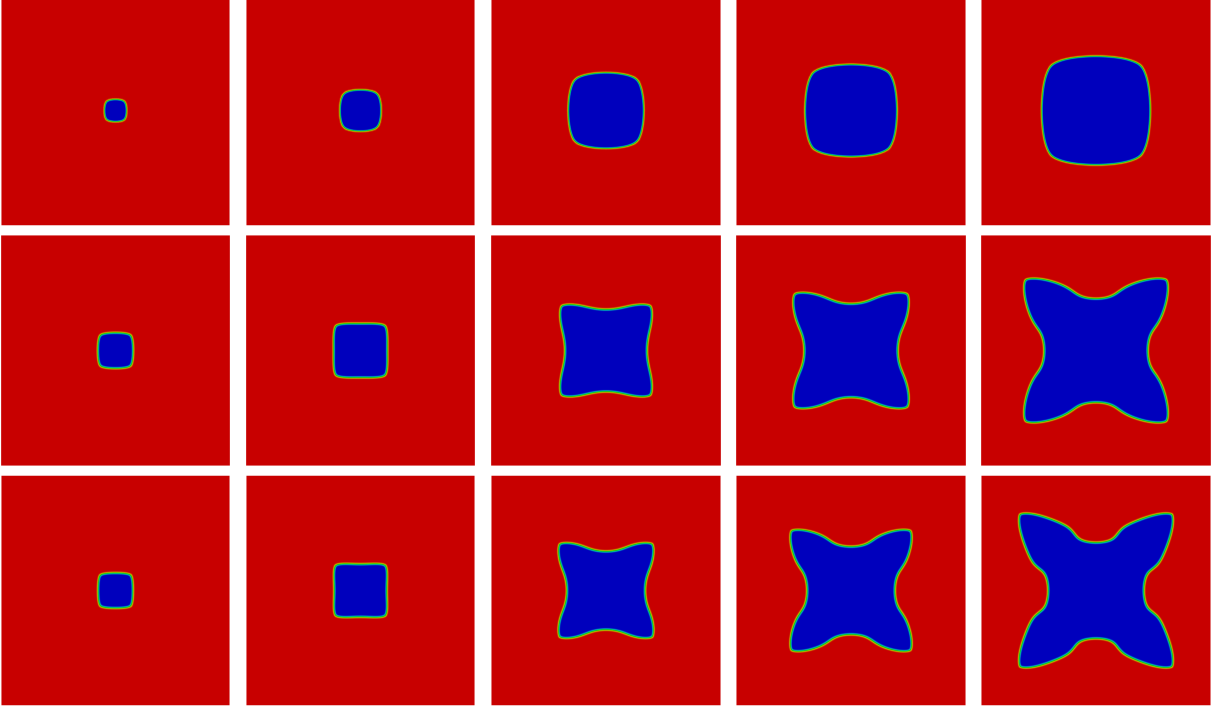


Figure 11: (PF_(ii)^{obs}-FEM, $\varepsilon^{-1} = 4\pi$, ANI₁, $\vartheta = 0$, $\alpha = 0.03$, $\rho = 0.01$, $u_D = -2$, $\Omega = (-8, 8)^2$) Snapshots of the solution at times $t = 1, 2, 4, 5, 6$. From top to bottom $\tau = 10^{-k}$, $k = 1 \rightarrow 3$. [These computations took 34 seconds, 7 minutes and 57 minutes, respectively.]

take at least 400 times as long.

For the next set of numerical experiments we use the hexagonal anisotropy

$$\text{ANI}_2: \quad \gamma(p) = \sum_{\ell=1}^3 l(R(\frac{\pi}{12} + \ell \frac{\pi}{3})p), \quad \text{where } l(p) = [p_1^2 + 10^{-4} p_2^2]^{\frac{1}{2}}, \quad (5.1)$$

and where $R(\theta) = \begin{pmatrix} \cos \theta & \sin \theta \\ -\sin \theta & \cos \theta \end{pmatrix}$ denotes a clockwise rotation through the angle θ . Moreover, we use the parameters $\vartheta = 1$, $\alpha = 5 \times 10^{-4}$, $\rho = 0.01$ and $u_D = -\frac{1}{2}$ on the boundary $\partial_D \Omega = \partial \Omega$ of $\Omega = (-2, 2)^2$. The radius of the initially circular seed is again chosen as $R_0 = 0.1$, and we set

$$u_0(x) = \begin{cases} 0 & |x| \leq R_0, \\ \frac{u_D}{1 - e^{R_0 - H}} (1 - e^{R_0 - |x|}) & R_0 < |x| < H, \\ u_D & |x| \geq H, \end{cases} \quad (5.2)$$

with $H := 2$.

Three numerical simulations for the scheme PF_(ii)^{obs}-FEM with the interfacial parameter $\varepsilon^{-1} = 16\pi$ can be seen in Figure 13. Observe that here we use a much smaller value of ε than previously, because for larger values of ε large mushy interfacial regions develop, which



Figure 12: (PFEM, ANI_1 , $\vartheta = 0$, $\alpha = 0.03$, $\rho = 0.01$, $u_D = -2$, $\Omega = (-8, 8)^2$) Snapshots of the solution at times $t = 1, 2, 4, 5, 6$. From top to bottom $\tau = 10^{-k}$, $k = 1 \rightarrow 3$. [These computations took 1, 6 and 73 seconds, respectively.]

means that the phase field simulations hold no value for the investigation of the underlying sharp interface problem. The creation of small localized mushy interfacial regions can be observed in Figure 13 for the run with $\tau = 10^{-3}$, while the run with $\tau = 10^{-4}$ shows larger such regions. In addition, in the latter run the phase field approximation of the growing crystal's surface reaches the external boundary $\partial\Omega$, which results in the creation of artificial, nonphysical interfaces. Repeating these simulations for a smaller interfacial parameter ε yields the results shown in Figure 14. Now for sufficiently small values of the time step size τ , the numerical results appear to be converging.

We also repeat the last computation for the scheme $\text{PF}_{(ii)}^{\text{obs}}$ -FEM with the explicit time discretization from (3.22a,b). Here any computation with a time step size $\tau \geq 10^{-5}$ was unstable, and so in Figure 15 we only show a run for $\tau = 10^{-6}$. We recall from Section 4.2, see Tables 6 and 7, that in the interest of accuracy uniform meshes should be employed for an explicit method. However, the large CPU times associated with a uniform grid mean that we are unable to complete the evolution within a reasonable amount of time. Hence in Figure 15 we use the same adaptive mesh strategy as in Figure 14 for the semi-implicit scheme $\text{PF}_{(ii)}^{\text{obs}}$ -FEM. Note that while the finest run in Figure 14 agrees well with the results shown in Figure 15, the very small time step size used for the latter means that the explicit scheme takes about 40 times as long as the semi-implicit scheme to compute the evolution. Hence, without further code optimizations, the explicit scheme would need to be run in parallel on a cluster with at least 40 nodes to become competitive.

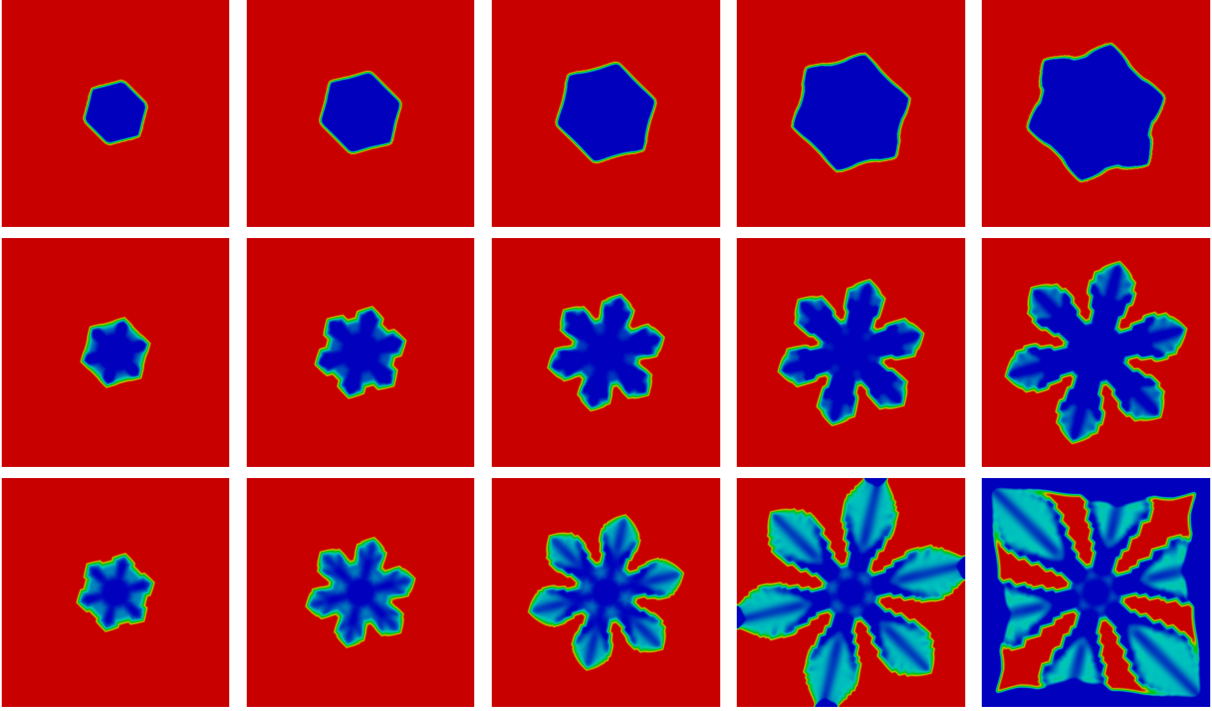


Figure 13: (PF_(ii)^{obs}-FEM, $\varepsilon^{-1} = 16\pi$, ANI₂, $\vartheta = 1$, $\alpha = 5 \times 10^{-4}$, $\rho = 0.01$, $u_D = -\frac{1}{2}$, $\Omega = (-2, 2)^2$) Snapshots of the solution at times $t = 0.3, 0.4, 0.5, 0.6, 0.7$. From top to bottom $\tau = 10^{-k}$, $k = 2 \rightarrow 4$. [These computations took 29 seconds, 26 minutes and 381 minutes, respectively.]

When we repeat the simulations shown in Figures 13 and 14 for the scheme PF_(iii)^{qua}-FEM, then in the run for $\varepsilon^{-1} = 16\pi$ large mushy interfacial regions appear, which quickly reach the boundary $\partial\Omega$. Hence we only present the simulations for $\varepsilon^{-1} = 32\pi$, see Figure 16, where we observe similar, but qualitatively quite different, results to the ones shown in Figure 14 for the scheme PF_(ii)^{obs}-FEM. In particular, the side arms in Figure 16 appear to be thinner than in Figure 14, and the convergence as τ gets smaller appears to be slower. We also repeat the computation from Figure 16 for the implicit time discretization from (3.20), see Figure 17. We observe that, in contrast to the conclusions that could be drawn from the isotropic experiments in Section 4, for the strongly anisotropic situation treated here there does not seem to be an advantage in using the implicit time discretization from (3.20) over the standard semi-implicit discretization (3.19a,b) from [16].

In addition, we present three simulations for the same physical problem for the sharp interface approximation PFEM in Figure 18, where we fix the spatial discretization parameters as $h_\Gamma \approx h_f = \frac{\sqrt{2}}{64}$. Here we observe once again that even for a very crude time discretization, the evolution is captured remarkably well, and there is very little variation in the numerical results from PFEM when τ is decreased. We also draw particular attention to the differing CPU times between the sharp interface calculations in Figure 18 and the phase field simulations in Figures 14–17.

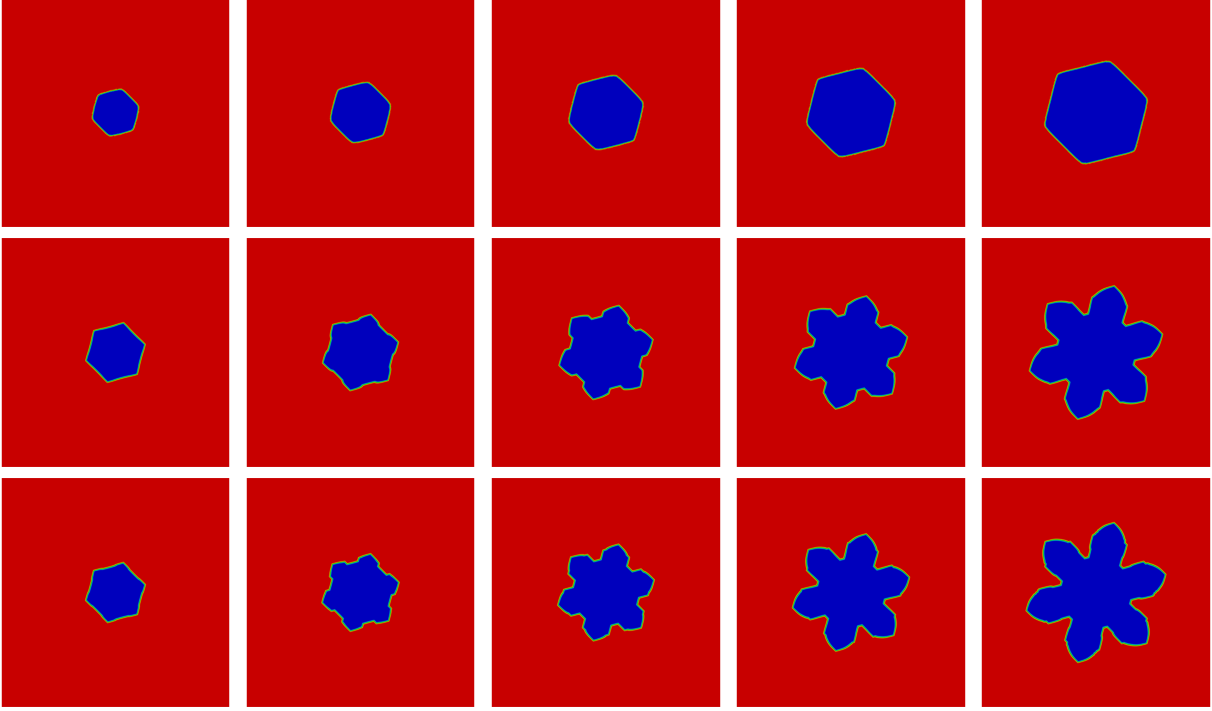


Figure 14: (PF_(ii)^{obs}-FEM, $\varepsilon^{-1} = 32\pi$, ANI₂, $\vartheta = 1$, $\alpha = 5 \times 10^{-4}$, $\rho = 0.01$, $u_D = -\frac{1}{2}$, $\Omega = (-2, 2)^2$) Snapshots of the solution at times $t = 0.3, 0.4, 0.5, 0.6, 0.7$. From top to bottom $\tau = 10^{-k}$, $k = 2 \rightarrow 4$. [These computations took 38 seconds, 8 minutes and 69 minutes, respectively.]

In the remainder of this section we consider two simulations for the scheme PFEM, which on present computer hardware are virtually impossible to repeat to a desirable accuracy with the phase field method. The first experiment is with the physical parameters from [14, Fig. 7], and so is for the one-sided quasi-stationary problem (2.3a–e) with $\vartheta = \mathcal{K}_- = 0$ and with γ as in (5.1). The remaining parameters are chosen as $\alpha = 10^{-5}$, $\rho = 1.42 \times 10^{-3}$ and $u_D = -0.04$ on the boundary $\partial_D \Omega = \partial \Omega$ of $\Omega = (-4, 4)^2$. The radius of the initially circular seed is chosen as 0.05. See Figure 19 for the results for different choices of the time step sizes τ , and with $h_\Gamma \approx h_f = \frac{\sqrt{2}}{128}$ fixed. We see that, as before, there is hardly any variation in the numerical results obtained from the three simulations with different values of τ for PFEM. Moreover, we note that due to the choice of the physical parameters much finer side branches appear in Figure 19 compared to the simulations in Figure 18. To precisely capture these small structures within a phase field computation would require very small values for the interfacial parameter ε , as well as correspondingly small discretization parameters h_f and τ ; recall (3.17), and (3.11). Taken together this means that we are currently unable to present phase field computations for an evolution as shown in Figure 19.

The next computation is similar to the simulation shown in [12, Fig. 14], where here we take as anisotropy

$$\text{ANI}_3: \quad \gamma(p) = ([g(p)]^9 + [g(R_1 p)]^9 + [g(R_2 p)]^9)^{\frac{1}{9}}, \quad \text{where } g(p) := [p_1^2 + \frac{1}{4}(p_2^2 + p_3^2)]^{\frac{1}{2}}, \quad (5.3)$$

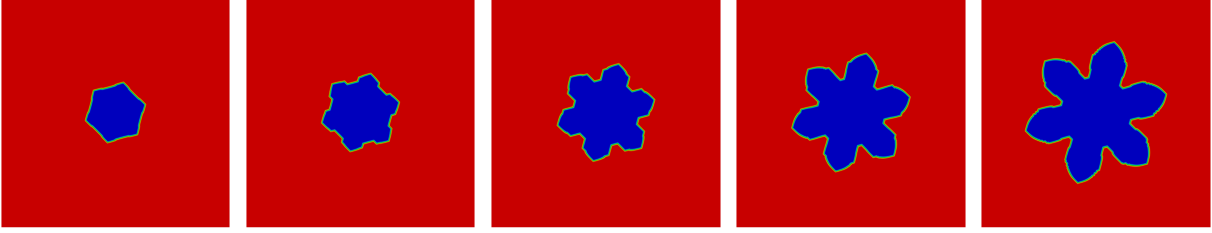


Figure 15: (PF_(ii)^{obs}-FEM with the explicit time discretization from (3.22a,b), $\varepsilon^{-1} = 32\pi$, ANI₂, $\vartheta = 1$, $\alpha = 5 \times 10^{-4}$, $\rho = 0.01$, $u_D = -\frac{1}{2}$, $\Omega = (-2, 2)^2$) Snapshots of the solution at times $t = 0.3, 0.4, 0.5, 0.6, 0.7$ for $\tau = 10^{-6}$. [This computation took 44 hours.]

with the two rotation matrices defined as $R_1 := \begin{pmatrix} 0 & 1 & 0 \\ -1 & 0 & 0 \\ 0 & 0 & 1 \end{pmatrix}$ and $R_2 := \begin{pmatrix} 0 & 0 & 1 \\ 0 & 1 & 0 \\ -1 & 0 & 0 \end{pmatrix}$. The

Wulff shape of the anisotropy (5.3) can be seen on the right of Figure 3 in [12]. Moreover, we use the parameters $\vartheta = 1$, $\alpha = 10^{-3}$, $\rho = 0.01$ and $u_D = -\frac{1}{2}$ on the boundary $\partial_D \Omega = \partial \Omega$ of $\Omega = (-4, 4)^3$. The radius of the initially spherical seed is chosen as $R_0 = 0.1$, and we let u_0 be defined by (5.2) with $H = 4$. Three simulations for these parameters, with the spatial discretization parameters fixed as $h_\Gamma \approx 5h_f = \frac{\sqrt{2}}{64}$, are presented in Figure 20. We observe that the three simulations all show the same general shape of the growing six-armed crystal, and for the smallest value of τ the results appear to have converged. We also note that the small oscillations in the solution for the simulation with the largest time step size disappear as τ is decreased. In order to demonstrate the good mesh properties of the parametric method PFEM, we show in Figure 21 two details of the triangulated approximation of $\Gamma(t)$ at times $t = 0.2$ and $t = 0.3$ for the finest time discretization in Figure 20. We recall that the algorithm PFEM does not employ any mesh-redistribution or mesh-smoothing methods. Rather it relies solely on local mesh refinements, where individual elements of the triangulation become too large, see [12, §5.2] for more details. The quality of the meshes shown in Figure 21 is excellent.

We recall that a simulation for the phase field algorithm PF_(ii)^{obs}-FEM for the same physical parameters has recently been performed in [16, Fig. 23]. As a comparison to the sharp interface calculations from Figure 20, we present the results for the scheme PF_(ii)^{obs}-FEM in Figure 22. We note that the evolution shown for the phase field approximation in Figure 22 is qualitatively very different from the sharp interface simulations in Figure 20. In all likelihood the physically challenging parameters for the computation in Figure 22 mean that, both in terms of the discretization parameters for the given $\varepsilon^{-1} = 16\pi$, e.g. the time step size τ , as well as in terms of the interfacial parameter ε itself, the shown numerical results are still far from the true underlying solution to the sharp interface problem (2.3a–e). Of course, a detailed numerical study into this question is not yet possible due to the long time that such computations would take.

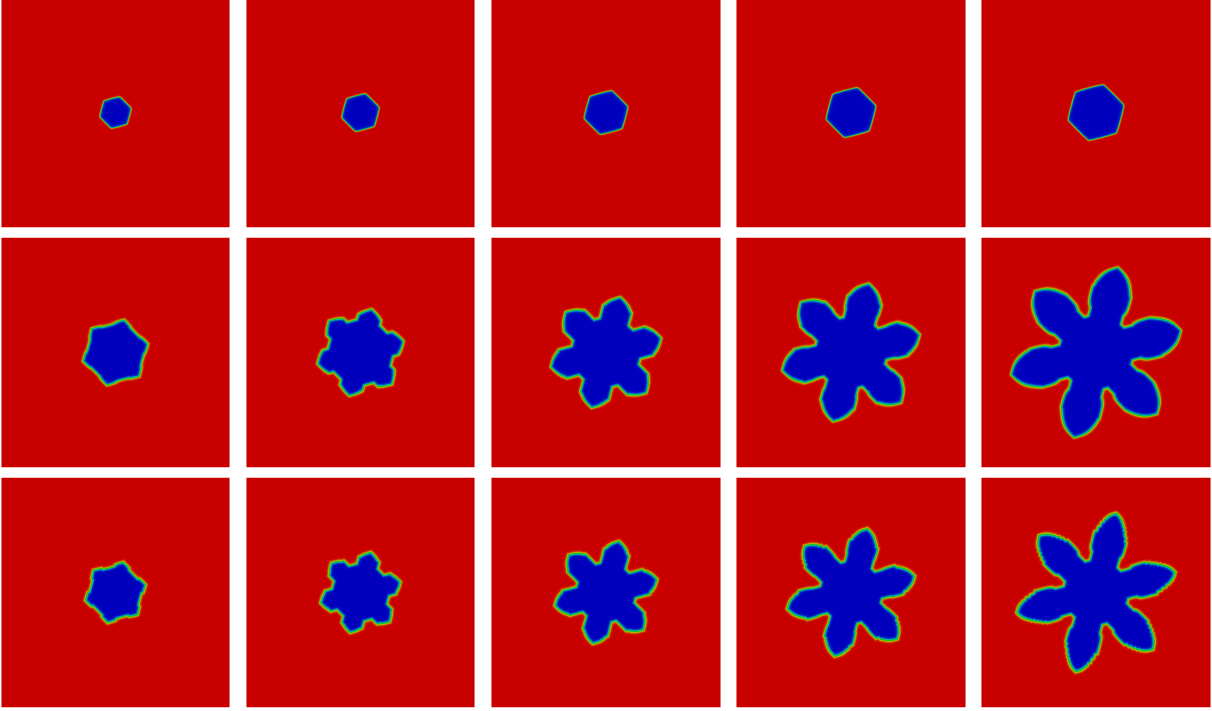


Figure 16: (PF_(iii)^{qua}-FEM, $\varepsilon^{-1} = 32\pi$, ANI₂, $\vartheta = 1$, $\alpha = 5 \times 10^{-4}$, $\rho = 0.01$, $u_D = -\frac{1}{2}$, $\Omega = (-2, 2)^2$) Snapshots of the solution at times $t = 0.3, 0.4, 0.5, 0.6, 0.7$. From top to bottom $\tau = 10^{-k}$, $k = 2 \rightarrow 4$. [These computations took 34 seconds, 16 minutes and 101 minutes, respectively.]

Conclusions

While numerical simulations for phase field models in general show qualitatively correct behaviour, often such numerical results are far away from the true sharp interface evolution. In order to obtain accurate simulations, the interface width ε , as well as the spatial and temporal discretization parameters need to be chosen sufficiently small. However, reducing these parameters to reach an acceptable accuracy often requires very large computing times on even the most advanced of today's desktop computers.

Direct sharp interface approximations, on the other hand, can provide a computationally cheap method to compute interface evolutions in materials science accurately. An example of such an algorithm is PFEM from [12, 13]. In the computations presented in this paper we have seen that even for very crude discretization parameters, the algorithm PFEM provides surprisingly accurate approximations. The computational time needed to compute these sharp interface approximations is often negligible compared to the CPU times necessary for a corresponding phase field simulation.

The main problem of phase field methods is that the asymptotic error in ε , which in general is not known, plays a significant role in determining the accuracy of phase field simulations. Small values of ε , in turn, require very small discretization parameters. Similarly,

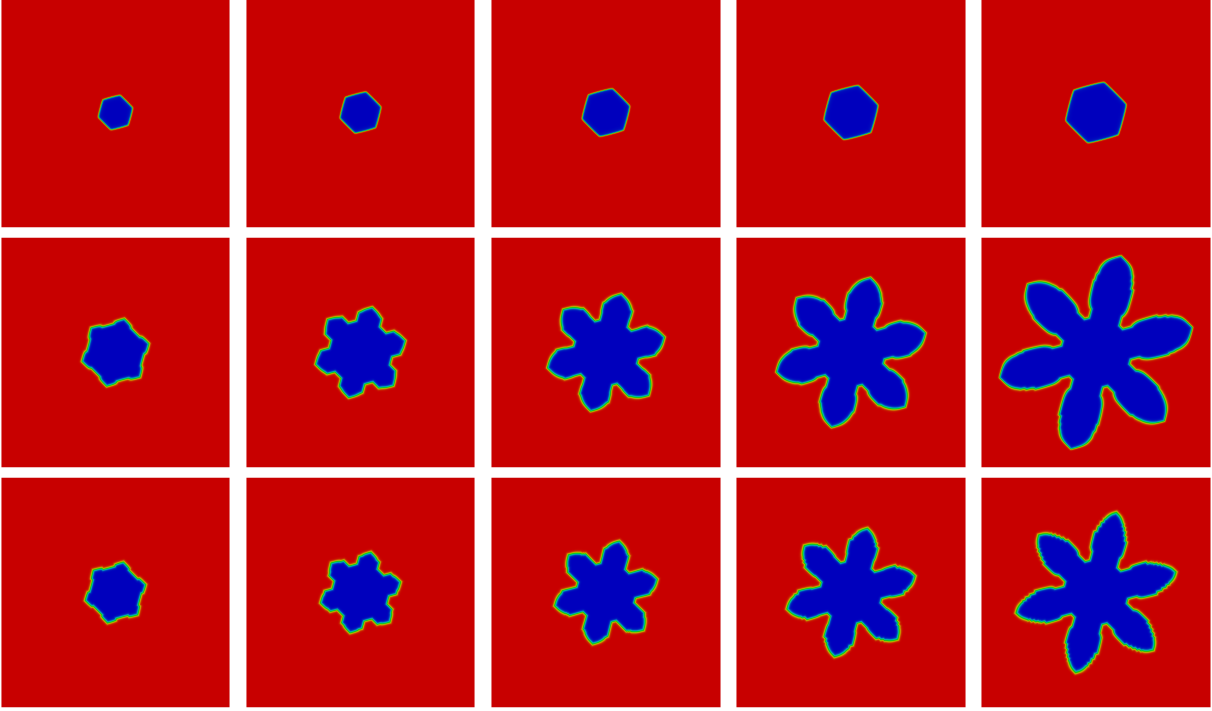


Figure 17: (PF_(iii)^{qua}-FEM with the implicit time discretization from (3.20), $\varepsilon^{-1} = 32\pi$, ANI_2 , $\vartheta = 1$, $\alpha = 5 \times 10^{-4}$, $\rho = 0.01$, $u_D = -\frac{1}{2}$, $\Omega = (-2, 2)^2$ Snapshots of the solution at times $t = 0.3, 0.4, 0.5, 0.6, 0.7$. From top to bottom $\tau = 10^{-k}$, $k = 2 \rightarrow 4$. [These computations took 43 seconds, 23 minutes and 119 minutes, respectively.]

in second order convergent isotropic phase field models with a correction term, where the asymptotic error in ε may be assumed to be relatively smaller than in classical phase field models, very small discretization parameters need to be employed in order to benefit from the smaller asymptotic error in practice. All of these issues do not arise in sharp interface approximations.

The main advantage of phase field methods over direct front tracking methods is that they intrinsically allow for topological changes. However, for the problem of solidification and dendritic growth as considered in this paper, topological changes in general do not occur during the simulation of physically relevant evolutions for single crystals.

In the past, researchers and scientists may have been discouraged from applying front tracking methods because of the difficulties in implementing such methods and because of the deterioration of the mesh quality as the approximated sharp interface evolves in time. However, assembling the system matrices in parametric finite element methods for evolving manifolds is not much different from the assembly in standard Cartesian problems, see e.g. [38, 39]. Of course, the coupling between a lower dimensional parametric mesh and a bulk mesh is nontrivial, but successful implementations have been used in e.g. [69, 70, 12, 13]. Moreover, the good mesh properties of the scheme PFEM from [12, 13] mean that a good mesh quality is maintained throughout the numerical simulations, and no remeshing is



Figure 18: (PFEM, ANI_2 , $\vartheta = 1$, $\alpha = 5 \times 10^{-4}$, $\rho = 0.01$, $u_D = -\frac{1}{2}$, $\Omega = (-2, 2)^2$) Snapshots of the solution at times $t = 0.3, 0.4, 0.5, 0.6, 0.7$. From top to bottom $\tau = 10^{-k}$, $k = 2 \rightarrow 4$. [These computations took 1, 9 seconds and 87 seconds, respectively.]

required in practice. In fact, all the simulations presented in this paper were performed without any remeshing, see [12] for more details.

We can summarize our main conclusions as follows:

- (C1) The parametric front tracking method PFEM is more accurate and computationally more efficient than phase field methods.
- (C2) For isotropic problems, implicit time discretizations for phase field models are often more accurate than semi-implicit time discretizations.
- (C3) Explicit time discretizations for phase field models need very small time steps in practice, and hence computations with explicit schemes are only competitive if run in parallel on large clusters.
- (C4) Second order accurate phase field models need finer discretization parameters than classical phase field models in order to demonstrate their superior approximation properties in practice.

Finally we note that while the focus of this paper has been the problem of dendritic solidification, it is to be expected that similar conclusions can be drawn when considering the respective merits of phase field models and sharp interface methods for other free boundary

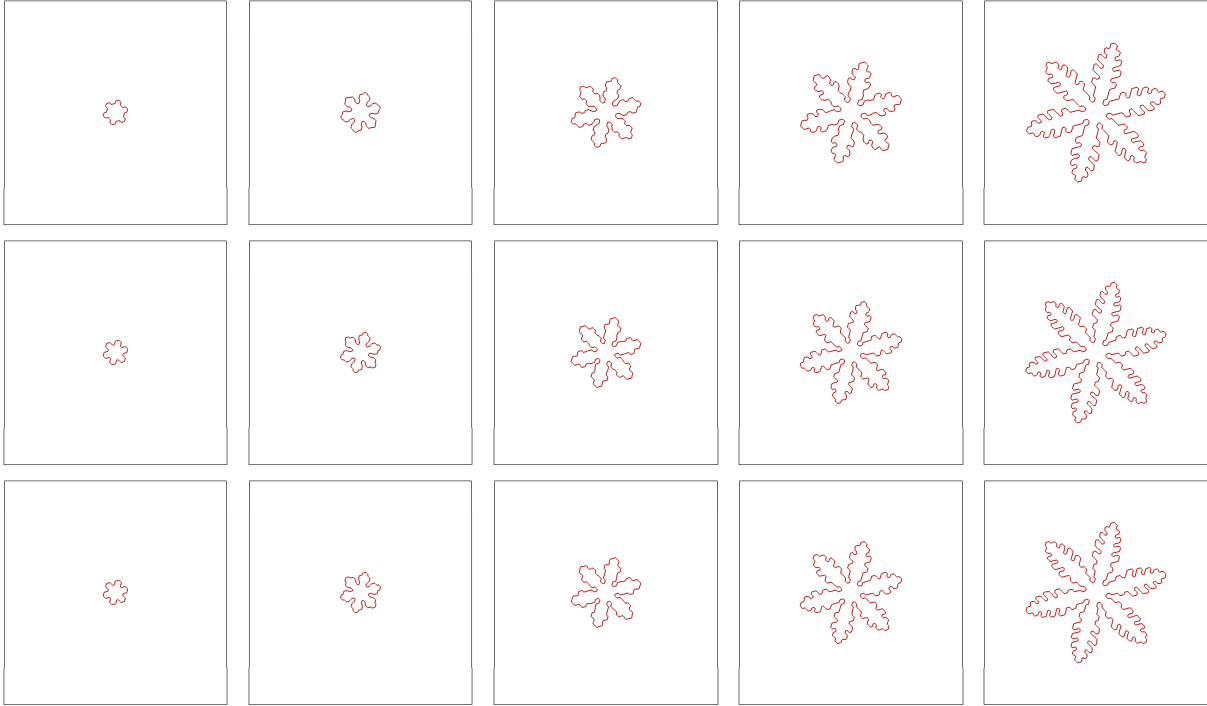


Figure 19: (PFEM, ANI_2 , $\vartheta = 0$, $\alpha = 10^{-5}$, $\rho = 1.42 \times 10^{-3}$, $u_D = -0.04$, $\Omega = (-4, 4)^2$) Snapshots of the solution at times $t = 5, 10, 20, 30, 40$. From top to bottom $\tau = 10^{-k}$, $k = 1 \rightarrow 3$. [These computations took 6, 124 and 781 minutes, respectively.]

problems in materials science, physics and biology. As possible examples we refer to epitaxial growth, surface diffusion, thermal grooving, sintering, vesicle dynamics and two phase flow.

It is our hope that the comparisons presented in this paper encourage a discussion about the merits of phase field methods in general, and of the possible advantages of using sharp interface approximations instead.

References

- [1] N. D. ALIKAKOS, P. W. BATES, AND X. F. CHEN, *The convergence of solutions of the Cahn–Hilliard equation to the solution of the Hele–Shaw model*, Arch. Rational Mech. Anal., 128 (1994), pp. 165–205.
- [2] R. F. ALMGREN, *Variational algorithms and pattern formation in dendritic solidification*, J. Comput. Phys., 106 (1993), pp. 337–354.
- [3] —, *Second-order phase field asymptotics for unequal conductivities*, SIAM J. Appl. Math., 59 (1999), pp. 2086–2107.
- [4] L. BAÑAS AND R. NÜRNBERG, *Finite element approximation of a three dimensional phase field model for void electromigration*, J. Sci. Comp., 37 (2008), pp. 202–232.

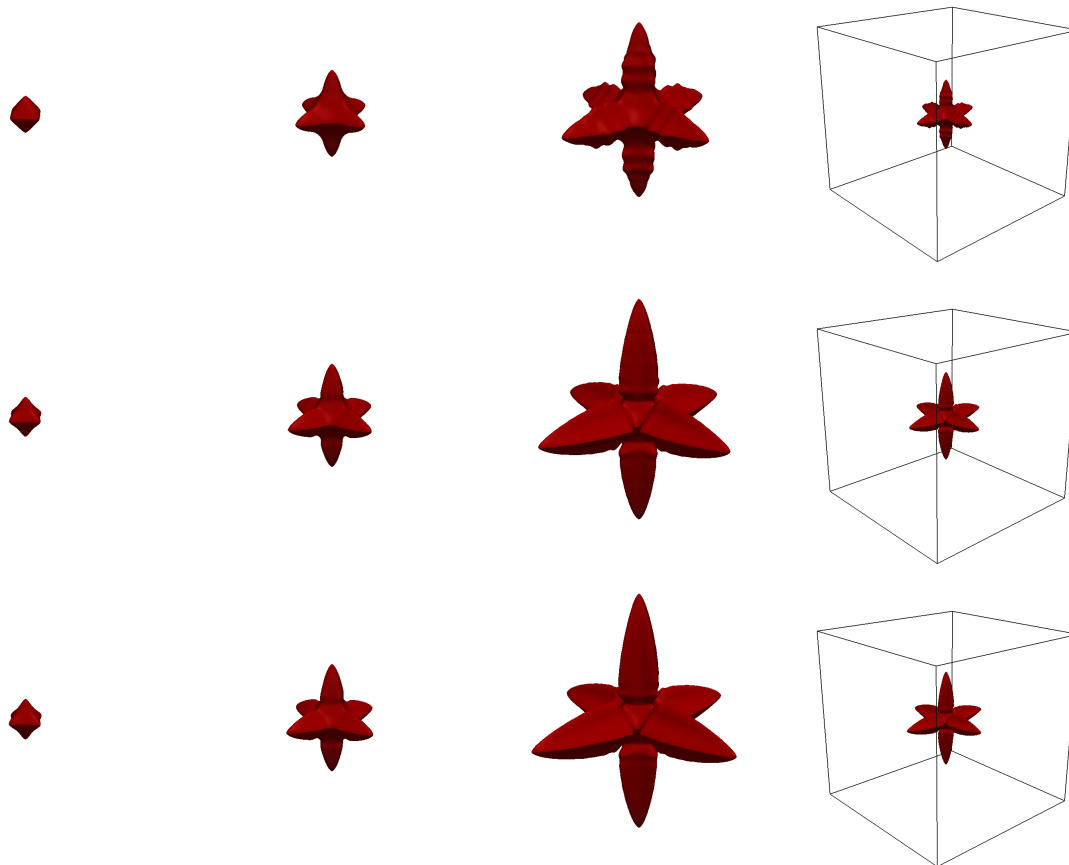


Figure 20: (PFEM, ANI_3 , $\vartheta = 1$, $\alpha = 10^{-3}$, $\rho = 0.01$, $u_D = -\frac{1}{2}$, $\Omega = (-4, 4)^3$) Snapshots of the solution at times $t = 0.1, 0.2, 0.3$, as well as the solution at time $T = 0.3$ within $\bar{\Omega}$. From top to bottom $\tau = 10^{-2}, 10^{-3}, 2 \times 10^{-4}$. [These computations took 2 hours, 20 hours and 50 hours, respectively.]

- [5] E. BÄNSCH AND A. SCHMIDT, *A finite element method for dendritic growth*, in Computational Crystal Growers Workshop, J. E. Taylor, ed., AMS Selected Lectures in Mathematics, 1992, pp. 16–20.
- [6] J. W. BARRETT, J. F. BLOWEY, AND H. GARCKE, *Finite element approximation of the Cahn–Hilliard equation with degenerate mobility*, SIAM J. Numer. Anal., 37 (1999), pp. 286–318.
- [7] J. W. BARRETT, H. GARCKE, AND R. NÜRNBERG, *On the variational approximation of combined second and fourth order geometric evolution equations*, SIAM J. Sci. Comput., 29 (2007), pp. 1006–1041.
- [8] —, *A parametric finite element method for fourth order geometric evolution equations*, J. Comput. Phys., 222 (2007), pp. 441–462.
- [9] —, *Numerical approximation of anisotropic geometric evolution equations in the plane*, IMA J. Numer. Anal., 28 (2008), pp. 292–330.

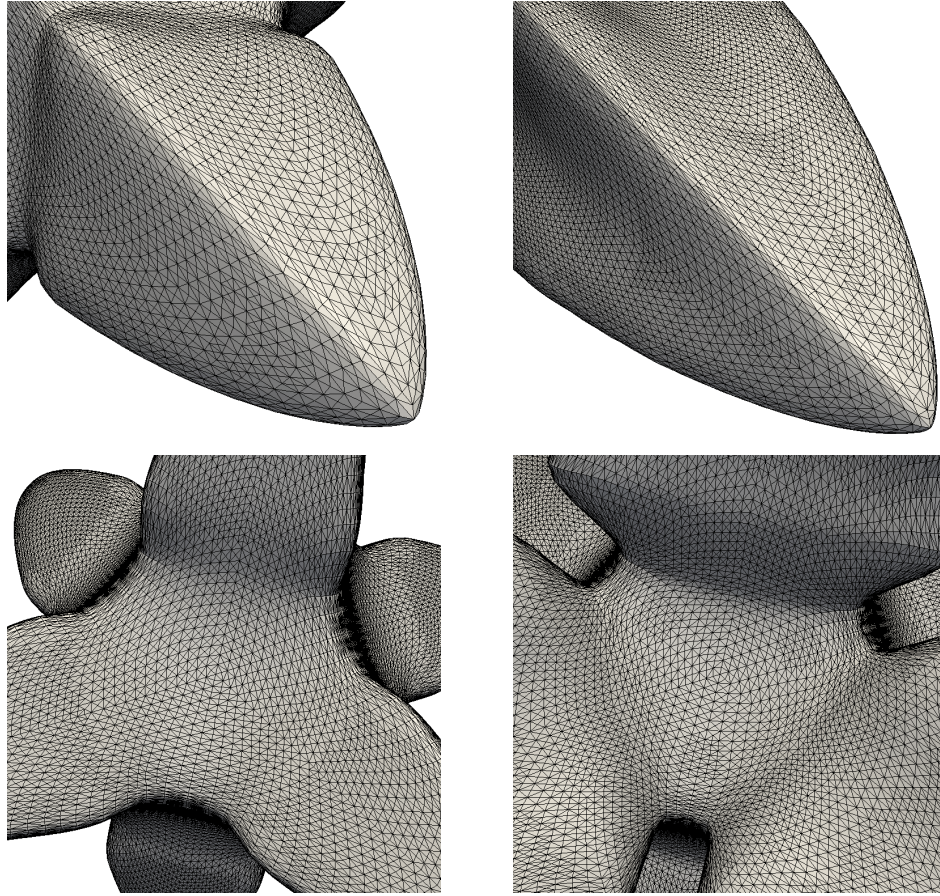


Figure 21: Details of the triangulations of PFEM in Figure 20 at times $t = 0.2$ (left) and $t = 0.3$ (right).

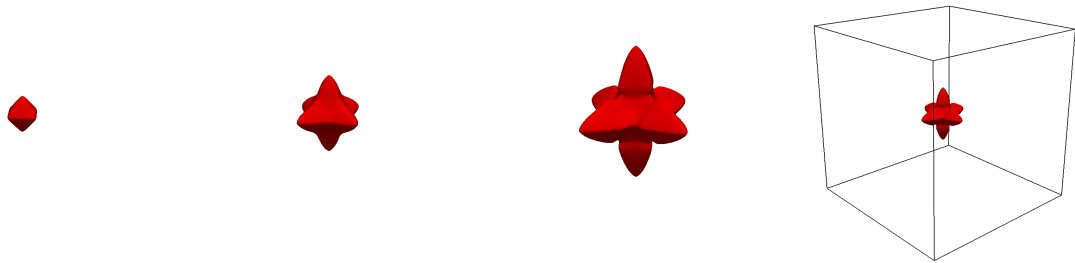


Figure 22: (PF_(ii)^{obs}-FEM, $\varepsilon^{-1} = 16\pi$, ANI₃, $\vartheta = 1$, $\alpha = 10^{-3}$, $\rho = 0.01$, $u_D = -\frac{1}{2}$, $\Omega = (-4, 4)^3$) Snapshots of the solution at times $t = 0.1, 0.2, 0.3$, as well as the solution at time $T = 0.3$ within $\bar{\Omega}$. This calculation uses $\tau = 10^{-4}$. [This computation took 8 days.]

- [10] —, *On the parametric finite element approximation of evolving hypersurfaces in \mathbb{R}^3* , J. Comput. Phys., 227 (2008), pp. 4281–4307.
- [11] —, *A variational formulation of anisotropic geometric evolution equations in higher dimensions*, Numer. Math., 109 (2008), pp. 1–44.
- [12] —, *On stable parametric finite element methods for the Stefan problem and the Mullins–Sekerka problem with applications to dendritic growth*, J. Comput. Phys., 229 (2010), pp. 6270–6299.
- [13] —, *Finite element approximation of one-sided Stefan problems with anisotropic, approximately crystalline, Gibbs–Thomson law*, Adv. Differential Equations, (2012). (to appear), see also <http://arxiv.org/abs/1201.1802>.
- [14] —, *Numerical computations of faceted pattern formation in snow crystal growth*, Phys. Rev. E, 86 (2012), p. 011604.
- [15] —, *On the stable discretization of strongly anisotropic phase field models with applications to crystal growth*, 2012. <http://arxiv.org/abs/1208.1147>.
- [16] —, *Stable phase field approximations of anisotropic solidification*, 2012. <http://arxiv.org/abs/1210.6791>.
- [17] S. BARTELS AND R. MÜLLER, *A posteriori error controlled local resolution of evolving interfaces for generalized Cahn–Hilliard equations*, Interfaces Free Bound., 12 (2010), pp. 45–73.
- [18] P. W. BATES, X. CHEN, AND X. DENG, *A numerical scheme for the two phase Mullins–Sekerka problem*, Electron. J. Differential Equations, 1995 (1995), pp. 1–28.
- [19] E. BEN-JACOB, *From snowflake formation to growth of bacterial colonies. Part I. Diffusive patterning in azoic systems*, Contemp. Phys., 34 (1993), pp. 247–273.
- [20] L. BLANK, M. BUTZ, AND H. GARCKE, *Solving the Cahn–Hilliard variational inequality with a semi-smooth Newton method*, ESAIM Control Optim. Calc. Var., 17 (2011), pp. 931–954.
- [21] L. BLANK, H. GARCKE, L. SARBU, AND V. STYLES, *Primal-dual active set methods for Allen–Cahn variational inequalities with non-local constraints*, Numer. Methods Partial Differential Equations, (2012). (DOI: 10.1002/num.21742, to appear).
- [22] J. F. BLOWEY AND C. M. ELLIOTT, *The Cahn–Hilliard gradient theory for phase separation with non-smooth free energy. Part II: Numerical analysis*, European J. Appl. Math., 3 (1992), pp. 147–179.
- [23] —, *A phase-field model with a double obstacle potential*, in Motion by mean curvature and related topics (Trento, 1992), G. Buttazzo and A. Visintin, eds., de Gruyter, Berlin, 1994, pp. 1–22.

- [24] W. J. BOETTINGER, J. A. WARREN, C. BECKERMANN, AND A. KARMA, *Phase-field simulation of solidification*, Annu. Rev. Mater. Res., 32 (2002), pp. 163–194.
- [25] G. CAGINALP, *An analysis of a phase field model of a free boundary*, Arch. Rational Mech. Anal., 92 (1986), pp. 205–245.
- [26] ———, *Stefan and Hele-Shaw type models as asymptotic limits of the phase-field equations*, Phys. Rev. A (3), 39 (1989), pp. 5887–5896.
- [27] G. CAGINALP AND X. CHEN, *Convergence of the phase field model to its sharp interface limits*, European J. Appl. Math., 9 (1998), pp. 417–445.
- [28] G. CAGINALP, X. CHEN, AND C. ECK, *Numerical tests of a phase field model with second order accuracy*, SIAM J. Appl. Math., 68 (2008), pp. 1518–1534.
- [29] G. CAGINALP AND J.-T. LIN, *A numerical analysis of an anisotropic phase field model*, IMA J. Appl. Math., 39 (1987), pp. 51–66.
- [30] J. W. CAHN AND D. W. HOFFMAN, *A vector thermodynamics for anisotropic surfaces – II. Curved and faceted surfaces*, Acta Metall., 22 (1974), pp. 1205–1214.
- [31] L.-Q. CHEN, *Phase-field models for microstructure evolution*, Annu. Rev. Mater. Res., 32 (2002), pp. 113–140.
- [32] X. CHEN, G. CAGINALP, AND C. ECK, *A rapidly converging phase field model*, Discrete Contin. Dynam. Systems, 15 (2006), pp. 1017–1034.
- [33] Z. M. CHEN AND K.-H. HOFFMANN, *An error estimate for a finite-element scheme for a phase field model*, IMA J. Numer. Anal., 14 (1994), pp. 243–255.
- [34] J. B. COLLINS AND H. LEVINE, *Diffuse interface model of diffusion-limited crystal growth*, Phys. Rev. B, 31 (1985), pp. 6119–6122.
- [35] S. H. DAVIS, *Theory of Solidification*, Cambridge Monographs on Mechanics, Cambridge University Press, Cambridge, 2001.
- [36] K. DECKELNICK, G. DZIUK, AND C. M. ELLIOTT, *Computation of geometric partial differential equations and mean curvature flow*, Acta Numer., 14 (2005), pp. 139–232.
- [37] G. DZIUK, *An algorithm for evolutionary surfaces*, Numer. Math., 58 (1991), pp. 603–611.
- [38] G. DZIUK AND C. M. ELLIOTT, *Finite elements on evolving surfaces*, IMA J. Numer. Anal., 27 (2007), pp. 262–292.
- [39] ———, *Surface finite elements for parabolic equations*, J. Comput. Math., 25 (2007), pp. 385–407.

- [40] C. M. ELLIOTT, *Approximation of curvature dependent interface motion*, in The state of the art in numerical analysis (York, 1996), I. S. Duff and G. A. Watson, eds., vol. 63 of Inst. Math. Appl. Conf. Ser. New Ser., Oxford Univ. Press, New York, 1997, pp. 407–440.
- [41] C. M. ELLIOTT AND A. R. GARDINER, *Double obstacle phase field computations of dendritic growth*, 1996. University of Sussex CMAIA Research report 96-19, <http://homepages.warwick.ac.uk/staff/C.M.Elliott/PAPERS/DoubleObstaclePhaseField/El1Gar96.pdf>.
- [42] C. M. ELLIOTT AND A. M. STUART, *The global dynamics of discrete semilinear parabolic equations*, SIAM J. Numer. Anal., 30 (1993), pp. 1622–1663.
- [43] X. FENG AND A. PROHL, *Analysis of a fully discrete finite element method for the phase field model and approximation of its sharp interface limits*, Math. Comp., 73 (2004), pp. 541–567.
- [44] G. J. FIX AND J. T. LIN, *Numerical simulations of nonlinear phase transitions. I. The isotropic case*, Nonlinear Anal., 12 (1988), pp. 811–823.
- [45] H. GARCKE AND B. STINNER, *Second order phase field asymptotics for multi-component systems*, Interfaces Free Bound., 8 (2006), pp. 131–157.
- [46] H. GARCKE, B. STOTH, AND B. NESTLER, *Anisotropy in multi-phase systems: a phase field approach*, Interfaces Free Bound., 1 (1999), pp. 175–198.
- [47] C. GRÄSER, R. KORNUBER, AND U. SACK, *Time discretizations of anisotropic Allen–Cahn equations*, 2011. Matheon Preprint, Berlin.
- [48] M. E. GURTIN, *Multiphase thermomechanics with interfacial structure. 1. Heat conduction and the capillary balance law*, Arch. Rational Mech. Anal., 104 (1988), pp. 195–221.
- [49] —, *Thermomechanics of Evolving Phase Boundaries in the Plane*, Oxford Mathematical Monographs, The Clarendon Press Oxford University Press, New York, 1993.
- [50] T. Y. HOU, J. S. LOWENGRUB, AND M. J. SHELLEY, *Removing the stiffness from interfacial flows with surface tension*, J. Comput. Phys., 114 (1994), pp. 312–338.
- [51] D. JURIC AND G. TRYGGVASON, *A front-tracking method for dendritic solidification*, J. Comput. Phys., 123 (1996), pp. 127–148.
- [52] A. KARMA AND W.-J. RAPPEL, *Phase-field method for computationally efficient modeling of solidification with arbitrary interface kinetics*, Phys. Rev. E, 53 (1996), pp. R3017–R3020.
- [53] —, *Quantitative phase-field modeling of dendritic growth in two and three dimensions*, Phys. Rev. E, 57 (1998), pp. 4323–4349.

- [54] D. A. KESSLER, J. KOPLIK, AND H. LEVINE, *Numerical simulation of two-dimensional snowflake growth*, Phys. Rev. A, 30 (1984), pp. 2820–2823.
- [55] R. KOBAYASHI, *Modeling and numerical simulations of dendritic crystal growth*, Phys. D, 63 (1993), pp. 410–423.
- [56] J. S. LANGER, *Models of pattern formation in first-order phase transitions*, in Directions in condensed matter physics, vol. 1 of World Sci. Ser. Dir. Condensed Matter Phys., World Sci. Publishing, Singapore, 1986, pp. 165–186.
- [57] J. T. LIN, *The numerical analysis of a phase field model in moving boundary problems*, SIAM J. Numer. Anal., 25 (1988), pp. 1015–1031.
- [58] S. LUCKHAUS, *Solutions for the two-phase Stefan problem with the Gibbs–Thomson law for the melting temperature*, European J. Appl. Math., 1 (1990), pp. 101–111.
- [59] G. B. MCFADDEN, *Phase-field models of solidification*, in Recent advances in numerical methods for partial differential equations and applications (Knoxville, TN, 2001), vol. 306 of Contemp. Math., Amer. Math. Soc., Providence, RI, 2002, pp. 107–145.
- [60] K. MIKULA AND D. ŠEVČOVIČ, *Evolution of plane curves driven by a nonlinear function of curvature and anisotropy*, SIAM J. Appl. Math., 61 (2001), pp. 1473–1501.
- [61] W. W. MULLINS AND R. F. SEKERKA, *Morphological stability of a particle growing by diffusion or heat flow*, J. Appl. Phys., 34 (1963), pp. 323–329.
- [62] B. NESTLER, *A 3D parallel simulator for crystal growth and solidification in complex alloy systems*, J. Cryst. Growth, 275 (2005), pp. e273–e278.
- [63] R. H. NOCHETTO AND C. VERDI, *Combined effect of explicit time-stepping and quadrature for curvature driven flows*, Numer. Math., 74 (1996), pp. 105–136.
- [64] —, *Convergence past singularities for a fully discrete approximation of curvature-driven interfaces*, SIAM J. Numer. Anal., 34 (1997), pp. 490–512.
- [65] S. OSHER AND R. FEDKIW, *Level Set Methods and Dynamic Implicit Surfaces*, vol. 153 of Applied Mathematical Sciences, Springer-Verlag, New York, 2003.
- [66] O. PENROSE AND P. C. FIFE, *Thermodynamically consistent models of phase-field type for the kinetics of phase transitions*, Phys. D, 43 (1990), pp. 44–62.
- [67] N. PROVATAS, N. GOLDENFELD, AND J. DANTZIG, *Efficient computation of dendritic microstructures using adaptive mesh refinement*, Phys. Rev. Lett., 80 (1998), pp. 3308–3311.
- [68] A. R. ROOSEN AND J. E. TAYLOR, *Modeling crystal growth in a diffusion field using fully faceted interfaces*, J. Comput. Phys., 114 (1994), pp. 113–128.
- [69] A. SCHMIDT, *Die Berechnung dreidimensionaler Dendriten mit Finiten Elementen*, PhD thesis, University Freiburg, Freiburg, 1993.

- [70] —, *Computation of three dimensional dendrites with finite elements*, J. Comput. Phys., 195 (1996), pp. 293–312.
- [71] —, *Approximation of crystalline dendrite growth in two space dimensions*, in Proceedings of the Algoritmy'97 Conference on Scientific Computing (Zuberec), J. Kačur and K. Mikula, eds., vol. 67, Bratislava, 1998, Slovak University of Technology, pp. 57–68.
- [72] J. A. SETHIAN, *Level Set Methods and Fast Marching Methods*, Cambridge University Press, Cambridge, 1999.
- [73] I. SINGER-LOGINOVA AND H. M. SINGER, *The phase field technique for modeling multiphase materials*, Rep. Progr. Phys., 71 (2008), p. 106501 (32 pages).
- [74] H. M. SONER, *Convergence of the phase-field equations to the Mullins–Sekerka problem with kinetic undercooling*, Arch. Rational Mech. Anal., 131 (1995), pp. 139–197.
- [75] I. STEINBACH, *Phase-field models in materials science*, Modelling Simul. Mater. Sci. Eng., 17 (2009), p. 073001.
- [76] B. E. E. STOTH, *Convergence of the Cahn–Hilliard equation to the Mullins–Sekerka problem in spherical symmetry*, J. Differential Equations, 125 (1996), pp. 154–183.
- [77] J. STRAIN, *A boundary integral approach to unstable solidification*, J. Comput. Phys., 85 (1989), pp. 342–389.
- [78] A. VEESER, *Error estimates for semi-discrete dendritic growth*, Interfaces Free Bound., 1 (1999), pp. 227–255.
- [79] S.-L. WANG, R. SEKERKA, A. WHEELER, B. MURRAY, S. CORIELL, R. BRAUN, AND G. MCFADDEN, *Thermodynamically-consistent phase-field models for solidification*, Phys. D, 69 (1993), pp. 189–200.
- [80] A. A. WHEELER, B. T. MURRAY, AND R. J. SCHAEFER, *Computation of dendrites using a phase field model*, Phys. D, 66 (1993), pp. 243–262.
- [81] X. Y. YUE, *Finite element analysis of the phase field model with nonsmooth initial data*, Acta Math. Appl. Sinica, 19 (1996), pp. 15–24.